1 **TITLE:** Modeling Synaptic Effects of Anesthesia and its Cortical Cholinergic Reversal

2

3

4 **AUTHORS:**

5 Bolaji P. Eniwaye [1,] Victoria Booth [2], Anthony G. Hudetz [1,3], Michal Zochowski [1,4]

6

7 **AUTHOR AFFILIATIONS:**

8 [1] Department of Applied Physics University of Michigan, 450 Church St, Ann Arbor, MI

9 48109

10 [2] Department of Mathematics, Department of Anesthesiology, University of Michigan, 530

11 Church St, Ann Arbor, MI 48109

12 [3] Center for Consciousness Science, Department of Anesthesiology, University of

13 Michigan, 1150 W Medical Center Dr, Ann Arbor, MI 48109

14 [4] Department of Physics, University of Michigan, 450 Church St, Ann Arbor, MI 48109

15 Corresponding Authors: Victoria Booth, Anthony G. Hudetz, Michal Zochowski;

16 vbooth@umich.edu, ahudetz@umich.edu, michalz@umich.edu

17

18

19   **Abstract:** General anesthetics work through a variety of molecular mechanisms while

20   resulting in the common end point of sedation and loss of consciousness. Generally, the

21   administration of common inhalation anesthetics induces decreases in synaptic excitation

22   while promoting synaptic inhibition. Animal studies have shown that, during anesthesia,

23   exogenously induced increases in acetylcholine-mediated effects in the brain can elicit

24   wakeful-like behavior despite the continued presence of the anesthetic. Less investigated,

25   however, is the question of whether the brain's electrophysiological activity is also

26   restored to pre-anesthetic levels and quality by such interventions. Here we apply a

27   computational model of a network composed of excitatory and inhibitory neurons to

28   simulate the network effects of changes in synaptic inhibition and excitation due to

29   anesthesia and its reversal by muscarinic receptor-mediated cholinergic effects. We use

30   a differential evolution algorithm to fit model parameters to match measures of spiking

31   activity, neuronal connectivity, and network dynamics recorded in the visual cortex of

32   rodents during anesthesia with desflurane *in vivo*. We find that facilitating muscarinic

33   receptor effects of acetylcholine on top of anesthetic-induced synaptic changes predicts

34   reversal of the neurons' spiking activity, functional connectivity, as well as pairwise and

35   population interactions. Thus, our model results predict a possible neuronal mechanism

36   for the induced reversal of the effects of anesthesia on post synaptic potentials, consistent

37   with experimental behavioral observations.

38

39

40

41

42

Author Summary

44 Here, we apply a computational model of a network composed of excitatory and inhibitory

45 neurons to simulate the network effects of changes in synaptic inhibition and excitation

46 due to anesthesia and we investigate the possibility of its reversal by muscarinic receptor-

47 mediated cholinergic effects. Specifically, we use a differential evolution algorithm to fit

48 model parameters to match dynamics recorded in the visual cortex of rodents during

49 anesthesia with desflurane *in vivo*. We find that changes of the fitted synaptic parameters

50 in response to the increasing desflurane concentration matched those established by

51 neurophysiology. Further, our results demonstrate that the cellular effects induced by

52 anesthesia can be mitigated by the changes in cellular excitability due to acetylcholine.

53

Introduction

55 Anesthesia is a pharmacological procedure that is used extensively in the medical

56 profession. The goal of anesthesia is typically to suppress the patient's conscious

57 awareness, stress and pain associated with surgery. Several putative mechanisms have

58 been proposed as to how anesthetic agents induce loss of awareness or consciousness,

59 however the variety of effects of different anesthetic agents within the central nervous

60 system make this an active area of study. Experimental studies implicate the brainstem,

61 thalamus, and cortex as regions where neuronal activity is heavily modified by general

62 anesthesia [1,2]. However, the primary target region likely depends on the type of

63 anesthetic [3]. At the single cell level, common inhalational anesthetics facilitate inhibitory

64   transmission and suppress excitatory synaptic transmission [4,5]. However, the extent of

65   effects on specific synaptic receptors varies across different anesthetics (Fig 1).

66

67   Despite such differences in direct effects of different anesthetic agents, an underlying

68   implicit hypothesis exists that there is an anesthetic agent-invariant mechanism that

69   accounts for their final effect, the loss of awareness or consciousness. Proposed neural

70   correlates of anesthetic action include modulation of neuronal excitability, increased

71   network synchrony [6], disrupted brain functional connectivity and deficits in information

72   integration [7,8]. Integrated Information Theory is one of the leading theories of

73   consciousness providing a general framework for how attention and awareness can be

74   attributed to transfer and processing of information within a system [9]. Supporting this

75   view, experimental studies have shown that information theoretic metrics of brain activity

76   are reduced during anesthesia associated with suppressed behavioral signs of

77   consciousness [10].

78

79   In order to understand the causal mechanisms of anesthetic action, additional

80   experimental manipulations have been performed to modulate the state of

81   consciousness. For example, pharmacological, electrical, and optogenetic stimulation of

82   various brain regions have been performed to counter or reverse the unconscious state

83   in humans and animals under the continued presence of anesthetic [11–14]. Many of

84   these investigations utilized nicotinic [15] or muscarinic [16] cholinergic interventions.

85   Recently, reverse dialysis delivery of the acetylcholine agonist carbachol was used to

86   successfully reverse the effect of sevoflurane in rats *in vivo* [17]. Similar effects were

87 observed *in vitro* when bathing cortical slices with cholinergic and noradrenergic agonists

88 led to a reversal of slow wave oscillations induced by anesthesia [18]. These studies have

89 shown that various behavioral expressions of the conscious state can be restored by

90 exogenous interventions that aim to counter the pharmacological effect of anesthetics.

91 Less investigated, however, is the question of whether the brain's electrophysiological

92 activity, particularly in cortical areas that are chiefly responsible for conscious

93 representations, are also restored to pre-anesthetic levels and quality by such

94 interventions. In other words, how do cortical neuronal activity patterns compare before

95 anesthesia, during anesthesia and after conscious-like behavior is restored by exogenous

96 stimulation while still in the presence of the anesthetic?

97

98 In the absence of such experimental measurements to date, computer simulations of

99 anesthetic effects on activity in neuronal network models present a useful and promising

100 approach. Here we embarked on such an investigation. In this study, we analyzed how

101 single-cell synaptic effects of anesthetics translate into mesoscale changes in population

102 dynamics that have been recorded in the visual cortex. We additionally investigated how

103 these changes may be reversed by cholinergic activation. To do this we simulated an

104 excitatory-inhibitory (E-I) neuron network consisting of biophysical model neurons with

105 glutamatergic, GABAergic and cholinergic inputs to model the effects of desflurane, a

106 common inhalation anesthetic, by varying the effect of excitatory and inhibitory

107 neurotransmitters in a manner consistent with experimentally observed effects of

108 desflurane at the synaptic level. To fit the model to experimentally obtained measures of

109 *in vivo* visual cortex network firing activity at different concentrations of desflurane, we

110 applied a differential evolution algorithm to optimize parameters modulating the effect of

111 neurotransmitter binding at different receptors. Specifically, we quantified the graded,

112 concentration-dependent effect of simulated anesthetic on neuronal firing rate

113 distributions, phase coherence, monosynaptic spike transmission, network functional

114 connectivity, and information theoretic measures of neuronal interactions, and fit these

115 measures to corresponding experimentally measured quantities in the rodent visual

116 cortex *in vivo*. We then used the model to simulate the presumed effect of cholinergic

117 activation, without changing parameters for the simulated anesthetic-induced synaptic

118 alterations, to see if these measures were reversible to near pre-anesthetic levels. Our

119 model results provide insight into the mechanisms by which distinct neurotransmitter

120 systems shape network behavior under the combined influence of complex

121 pharmacological interventions that may affect the state of consciousness.

122

123

124

Fig 1. Common inhalation anesthetics have similar effects on synaptic receptors. Experimental findings show similar effects across inhalation anesthetics on synaptic receptors [19,20]. Binding to inhibitory GABA$_A$ receptors is commonly potentiated while NMDA receptor activity is commonly inhibited with the magnitude of effect varying between anesthetics. Activation of muscarinic acetylcholine receptors and AMPA receptors is inhibited by isoflurane and sevoflurane while desflurane has a biphasic effect and null effect on muscarinic acetylcholine and AMPA receptors, respectively.

Results

We constructed a reduced, biophysical, neuron network model to investigate how synaptic-level changes, mediated by the anesthetic desflurane, affect network-level dynamics compared to data measured in the visual cortex *in vivo*, and, separately, how cholinergic neuromodulatory changes at the cellular level may reverse these anesthetic effects. The network consisted of excitatory and inhibitory neurons interacting via synapses mediated by excitatory AMPA and NMDA receptors and inhibitory GABA$_A$ receptors (see Methods section Fig 8). In addition, excitability of excitatory cells was

141   modulated by acetylcholine (ACh), implemented via the ACh-dependent slow,

142   hyperpolarizing K+ M-current.

143

144   We used an evolutionary algorithm (see Methods section, Fig 11) to identify optimal

145   synaptic connectivity parameter sets (Table 1/Table 2) that most closely match multiple

146   quantitative measures of network activity recorded under different desflurane

147   concentrations. This allowed us to objectively find two sets of parameter modifications

148   that fit model results to the experimental data. Namely, in one set of optimized

149   parameters, we allowed the algorithm to optimize the inhibitory GABA$_A$ connectivity

150   strength and excitatory NMDA connectivity strength while keeping AMPA connectivity

151   strength constant as simulated anesthetic concentration was increased (Table 1/Table 2,

152   A-Series). In the second set, in addition to varying the above parameters, we allowed

153   cholinergic effects to vary with simulated anesthetic concentration (Table 1/Table 2, B-

154   Series). The optimization was based on fitting measures of network frequency, mean

155   phase coherence, and information theoretic measures of integration and complexity, and

156   the parameter sets were validated using measures of synaptic connection probability and

157   strength, as well as network functional connectivity (see Methods section, Fig 7).

158   Optimizations were conducted separately for each anesthetic level, i.e., parameter values

159   A1/B1 were optimized to data recorded for 0% desflurane concentration, A2/B2 for 2%

160   desflurane, A3/B3 for 4% desflurane and A4/B4 for 6% desflurane.

161   In each optimization run we kept the network structure fixed. Particularly, when optimizing

162   across the A-series/B-series we maintained a single network to guarantee that the cost

163   or loss function monotonically decreased across generations. To check for robustness,

164   we optimized parameters for 10 independent network realizations. For each network

165   optimization, the initial pool of parameters seeding the search was kept the same. Table

166   1 reports mean and standard error of obtained parameter values of the 10 optimization

167   runs. Table 2, on the other hand, represents the single optimized parameter set that was

168   subsequently used to identify anesthetic effects on the dynamics of the network.

169

170   With synaptic connectivity parameters fixed at their levels corresponding to 6% desflurane

171   concentration, we then simulated the reversal of the anesthetic effects by increasing AÇh

172   effects as mediated by the muscarinic receptor dependent M-type K+ current (specifically,

173   decreasing its conductance g_{Ks}; Table 2, AR/BR-Series).

174

175   The synaptic connectivity parameter values determined by the evolutionary algorithm

176   mirrored experimentally identified effects of desflurane on excitatory and inhibitory

177   synaptic currents (See Methods section, Fig 11). For example, in the A-series

178   parameters, there was a decrease in the effects of NMDA receptor-mediated current while

179   there was an increase in the effect of GABA-mediated current in response to increases

180   in anesthesia (Table 1/Table 2). A similar trend was obtained in the B-Series with the

181   added result that decreasing effects of acetylcholine (increasing g_{Ks}) correlated to the

182   effects of increased anesthesia except for the change from B3 to B4. Interestingly, the

183   optimization predicted that, in the B-Series, to offset the decrease in neuronal excitability

184   due to decreasing ACh level (i.e., increased g_{Ks}) with anesthetic concentration, the

185   increase in $GABA_A$ synaptic efficacy was smaller than that obtained in the A-Series, and

186   similarly, the NMDA synaptic efficacy was systematically higher as compared to the A-

187   Series.

188

189   Fig 2 shows example raster plots comparing experimental spike timing data collected

190   under the varying desflurane concentrations with model results for the optimized A- and

191   B-Series parameter sets, as well as the simulated ACh-induced reversal of anesthetic

192   effects. The model raster plots show similar qualitative trends for increasing simulated

193   anesthetic concentration as the experimental data, specifically spiking patterns change

194   from asynchronous with higher spiking frequencies at simulated 0% desflurane

195   concentration (A1/B1) to a lower frequency, more synchronized firing pattern for

196   simulated 6% desflurane concentration (A4/B4). Furthermore, the simulated ACh reversal

197   (AR1/BR1 – AR4/BR4) reverses those trends.

198

199   In the following sections, we analyze how specific characteristics and measures of

200   network dynamics, including frequency distributions and profiles, mean phase coherence,

201   information theoretic measures, and excitatory/inhibitory connectivity probability,

202   computed for the experimental data for progressively increased desflurane levels are

203   reproduced in the optimized model networks. These measures were then computed for

204   simulated increasing levels of cholinergic modulation to analyze the recovery of network

205   dynamics during ACh-induced reversal of anesthetic effects.

206

207

208

209

210

	P_{NMDA}	P_{GABA}	P_{AMPA}	g_{Ks}		P_{NMDA}	P_{GABA}	P_{AMPA}	g_{Ks}
	A-Series ($\pm$SEM)					**B-Series** ($\pm$SEM)			
A1	**1.69** $\pm$0.05	**3.92**$\pm$0.51	**1.27**$\pm$0.67	**0.98**$\pm$0.08	B1	**1.69** $\pm$.0.05	**3.92** $\pm$0.51	**1.27**$\pm$0.67	**0.98**$\pm$0.08
A2	**1.41** $\pm$0.03	**4.32**$\pm$0.44	**1.27** -	**0.98** -	B2	**1.63** $\pm$0.07	**5.51**$\pm$0.33	**1.27** -	**1.07**$\pm$0.03
A3	**1.22**$\pm$0.12	**8.13**$\pm$1.21	**1.27** -	**0.98** -	B3	**1.47** $\pm$0.06	**6.35**$\pm$0.94	**1.27** -	**1.23**$\pm$0.02
A4	**1.09**$\pm$0.09	**10.61**$\pm$1.91	**1.27** -	**0.98** -	B4	**1.36** $\pm$0.09	**8.17**$\pm$1.41	**1.27** -	**1.17**$\pm$0.06

211
212
213
214 **Table 1. Parameter optimization for simulated anesthetic concentrations when**
215 **performed on 10 different network realizations.** A/B-series describe optimal values
216 determined by the differential evolution algorithm fitting network connectivity parameters
217 obtained when repeating the optimization for 10 total networks. Optimization includes A-
218 Series, when ACh effects are assumed constant and B-Series, when ACh effects are
219 allowed to change with anesthetic concentration. The scaling factors P_x scale the effects
220 of synaptic conductances mediated by the x receptor (x = NMDA, GABA and AMPA). A1-
221 A4/B1-B4 denote optimal parameter sets fit to experimental recordings at varying
222 anesthetic concentrations (0%, 2%, 4%, 6% desflurane, respectively). P_{AMPA} is only fit for
223 the 0% anesthetic case A1/B1. Error displayed is SEM.
224

225
226

	P_{NMDA}	P_{GABA}	P_{AMPA}	g_{Ks}		P_{NMDA}	P_{GABA}	P_{AMPA}	g_{Ks}
	A-Series					**B-Series**			
A1	1.64	4.51	1.19	0.94	B1	1.64	4.51	1.19	0.94
A2	1.46	5.63	1.19	0.94	B2	1.58	5.32	1.19	1.12
A3	1.39	6.72	1.19	0.94	B3	1.44	5.81	1.19	1.24
A4	1.26	7.63	1.19	0.94	B4	1.34	7.51	1.19	1.21
	A-Series Reversal					**B-Series Reversal**			
AR1	1.26	7.63	1.19	0.81	BR1	1.34	7.51	1.19	1.01
AR2	1.26	7.63	1.19	0.67	BR2	1.34	7.51	1.19	0.81
AR3	1.26	7.63	1.19	0.53	BR3	1.34	7.51	1.19	0.60
AR4	1.26	7.63	1.19	0.40	BR4	1.34	7.51	1.19	0.40

227

228 **Table 2. Parameter values for simulated anesthetic concentrations and cholinergic**
229 **reversal results.** Parameters from initial fit used to simulate anesthetic effects and
230 cholinergic reversal. A/B-series describe optimal values of initial fit determined by the
231 differential evolution algorithm for network connectivity parameters obtained when ACh
232 effects are assumed constant (i.e., g_{Ks} is constant; A-Series) and when ACh effects are
233 allowed to change with anesthetic concentration (B-Series). P_x denotes scaled changes
234 in synaptic conductance's mediated by the x receptor (x = NMDA, GABA and AMPA) as
235 described in Table 1. A/B-Series Reversal (AR/BR series) represent simulated anesthetic
236 reversal, obtained by increasing ACh effects (decreasing g_{Ks} from A4/B4 levels) while
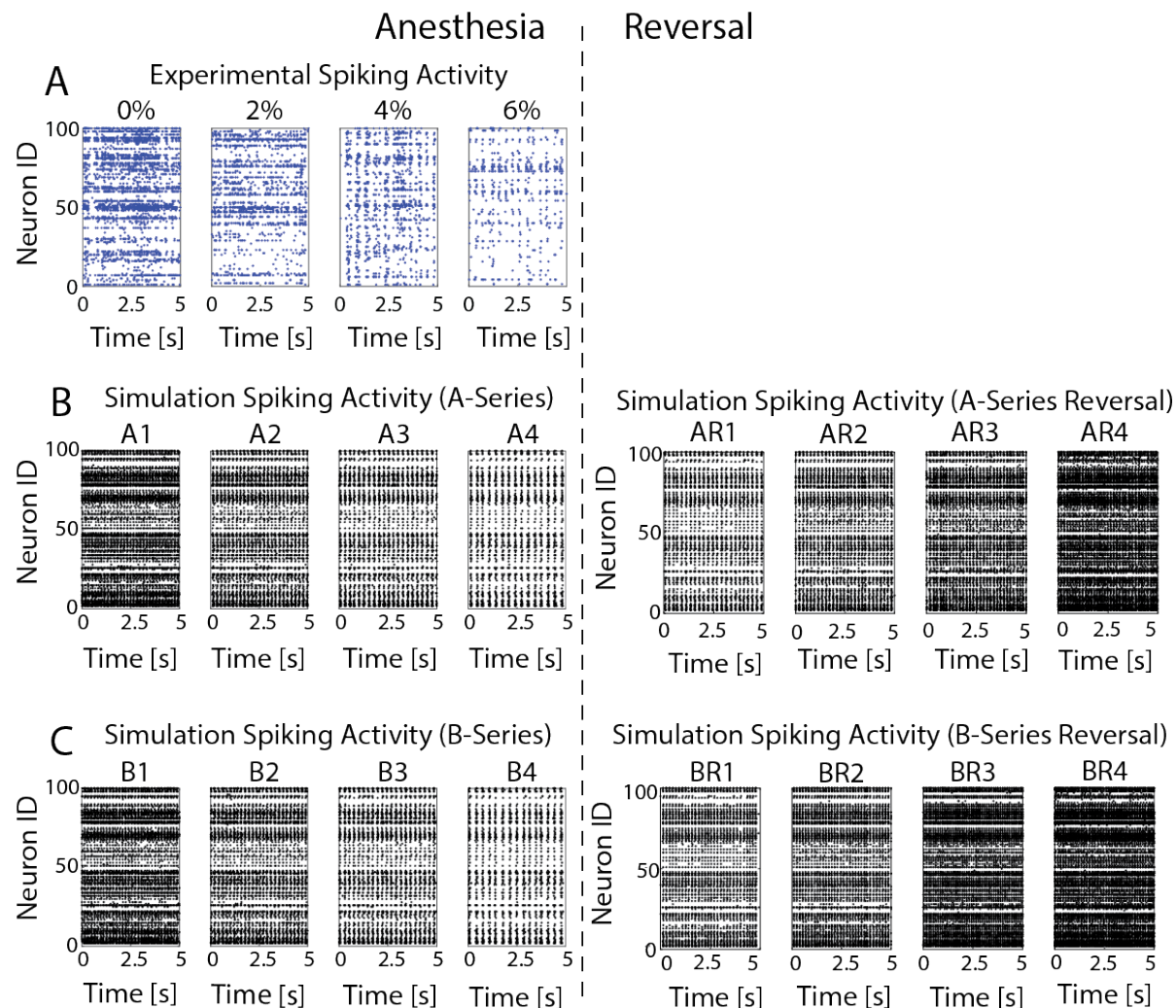237 keeping all other parameters constant.
238

239

Fig 2. Changes in anesthesia level lead to transitions from high frequency asynchronous to low frequency synchronous spiking patterns A) Raster plots of experimentally recorded neuronal activity in response to changes in desflurane levels. For higher concentrations of desflurane (**6%**), oscillatory synchronous network activity can be seen in spiking dynamics. For lower levels of anesthetic, oscillations are not apparent and asynchronous activity dominates. **B)** Raster plots for simulated anesthetic effects in optimized model networks for constant g_{Ks} (A series) and the simulated ACh-induced reversal of anesthetic effects (A series reversal). **C)** Raster plots for simulated anesthetic effects in optimized networks with changing g_{Ks} (B-series) and its reversal (B series reversal). In both B) and C), simulated anesthetic reversal shows reinstatement of asynchronous from synchronous spiking patterns.

255   **Anesthetic effects on network dynamics and their predicted ACh-induced reversal**

256   Anesthetic and reversal effects on spike frequencies

257   We first characterized the changes in the mean neuronal spike frequency as well as the

258   shape of the neuronal spike frequency distributions as a function of anesthetic level in the

259   optimized model networks (Fig 3 and Fig 4A). We observed that the neurons generally

260   fired less, in both experimental data and the simulations, as a function of anesthetic

261   concentration. Also, the spread of neuronal firing frequencies decreased significantly with

262   increased anesthetic level, with the loss of the right skew observed in the wake cases

263   (0%, A1 and B1). Spike frequency decreased as a function of desflurane levels for both

264   parameter series, (A and B series, without and with ACh changes, respectively), with a

265   similar frequency drop, irrespective of the implemented ACh changes that affect neuronal

266   excitability in the B series. In predicted ACh-induced reversal, the rightward skew in

267   frequency distributions was recovered, and the B series showed stronger recovery in

268   mean spike frequency as compared to the A series. This is because, as mentioned above,

269   accounting for cholinergic changes on neuronal excitability under desflurane anesthesia

270   predicts that synaptic changes are less severe. Namely, in the B series, $GABA_A$ synaptic

271   strength was not as high, and NMDA synaptic was not as low compared to the A series.
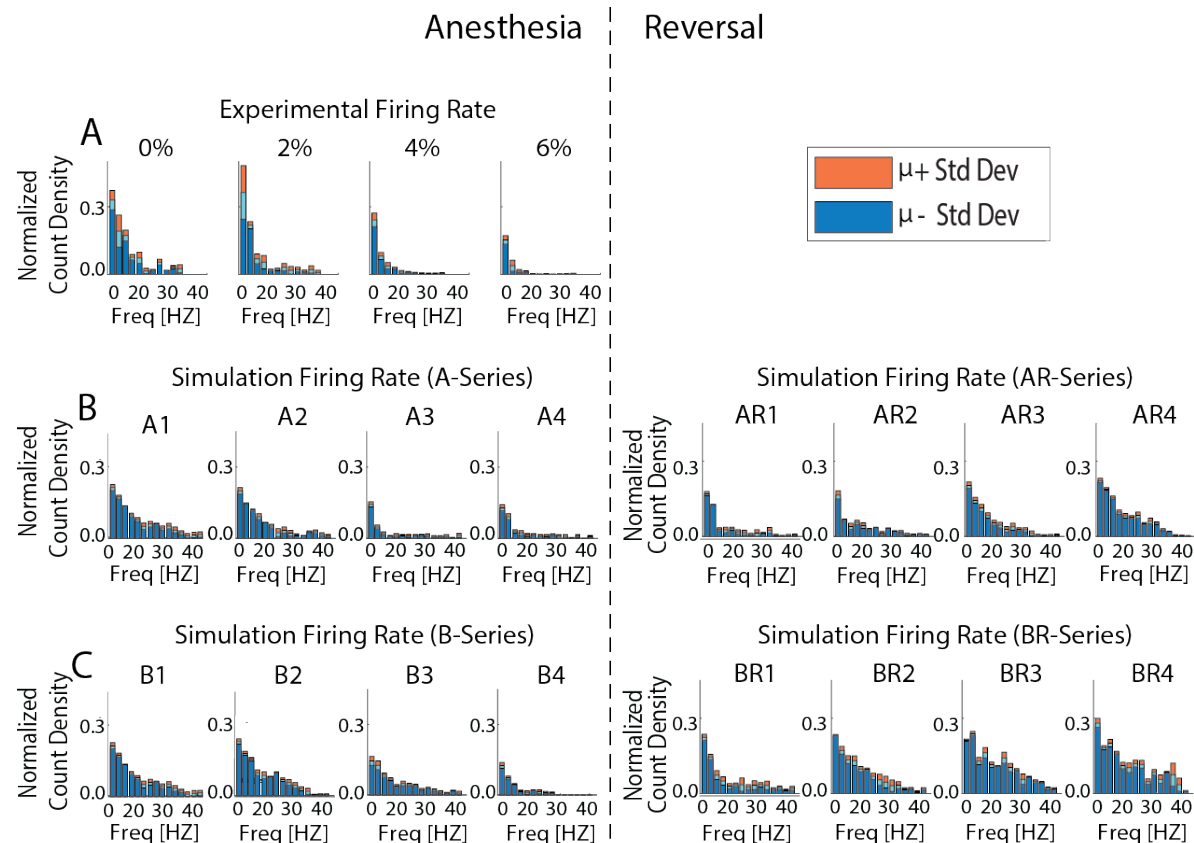
272

Fig 3. Firing rate distributions for different levels of anesthetic concentration. A) Changes in experimentally recorded firing rate distributions under increasing desflurane concentration (0, 2, 4, and 6%) show increased right skewness for the awake state in comparison to anesthetic states. The bins were normalized by the total number of spikes relative to the awake case (0%). **B) and C)** Firing rate distributions in optimized networks for A (B) and B (C) series parameter sets. Simulated networks show similar trends in frequency distributions when compared to experiment. The predicted ACh-induced reversal shows reinstatement of the right skew. The bins were normalized by the total number of spikes relative to the awake case A1/B1. Upper/Lower bound show histogram standard deviation.

Anesthetic and reversal effects on network synchrony

In both experimental and simulated results, the common feature was an increase in network synchronization as a function of increased desflurane levels. Mean phase coherence (MPC) measures the consistency of the relative phase that neurons fire with respect to each other thus taking into account non-zero time lag synchrony. For both the

291   experimental data and the optimized network simulations, the mean phase coherence

292   was lowest at the 0% anesthesia case and increased with increasing anesthetic

293   concentration (Fig 4B). For higher levels of anesthesia, while the simulations and the

294   experimental data showed increasing MPC, simulated networks exhibited a larger

295   increase. This could be due to the fact that our model only represents local network

296   interactions, without incorporating the existence of external inputs that could additionally

297   desynchronize the network activity. In the visual cortex, there are non-local network

298   inputs possibly preventing a high level of synchronization in the locally recorded network

299   activity.

300

301   The anesthetic reversal with increased levels of ACh (i.e. decreased g_{Ks}) led to decreases

302   in MPC indicating desynchronization in network activity. This is not suprising, as

303   decreased M-current leads to larger differentiation in neuronal firing rate as a function of

304   external input and changes in the phase response curves (PRCs), which also promote

305   desynchronisation for lower g_{KS} [21].

306

307   <u>Anesthetic and reversal effects on network information metrics</u>

308   We computed the information theoretic measures network integration (I(X)) and

309   complexity (C(X)) for both experimental data and simulated network activity. Integration

310   I(X) is a generalization of mutual information that measures the amount of total entropy

311   of a system that is accounted for by the interactions among its elements. I(X) is zero when

312   system elements are statistically independent [22]. Complexity C(X), on the other hand,

313   measures the total entropy loss due to interaction of system elements, or, equivalently,

314 the difference between the sum of the entropies of the individual elements and the entropy

315 of the entire system. C(X) is low for systems with independent elements or with highly

316 synchronous elements.

317

318 To compute the integration and complexity measures, 60 neurons were selected at

319 random from both the experimental data and the simulated networks. The spike trains

320 were then binned with 1ms bins to form binary activity vectors. I(X) and C(X) were

321 computed by taking 3 random intervals of 6s, computing the measure on each set of

322 intervals and then averaging the measure outcomes across the three sets (see Methods

323 section for a detailed description). I(X) and C(X) displayed similar changes in both the

324 experiment and simulations with increasing anesthetic concentration (Fig 4C,D). Namely,

325 both measures decreased as a function of the anesthetic level. A difference in trends

326 between simulation results of the A and B series is evident here, with the A series

327 exhibiting a significantly more precipitous drop in both measures with increasing

328 anesthetic level, as compared to the B-series. This again can be explained by the

329 differences in network connectivity parameters (i.e., NMDA and $GABA_A$ synaptic

330 strengths) obtained for the two series. Specifically, lower NMDA synaptic efficacy and

331 higher GABA synaptic efficacy leads to effective disconnection of the neurons in the A

332 series networks, resulting in lower I(X) and C(X) measures.

333

334 Simulated ACh-induced reversal acted to increase both these measures (Fig 4C,D;

335 AR/BR series). In the B series reversal, both measures recovered to values greater than

336 the simulated waking values A1/B1. This was due to the higher NMDA and lower $GABA_A$

337   synaptic efficacies that lead to significantly stronger excitatory interactions between the

338   neurons in the B-series simulations, increasing I(X) and C(X) measures.
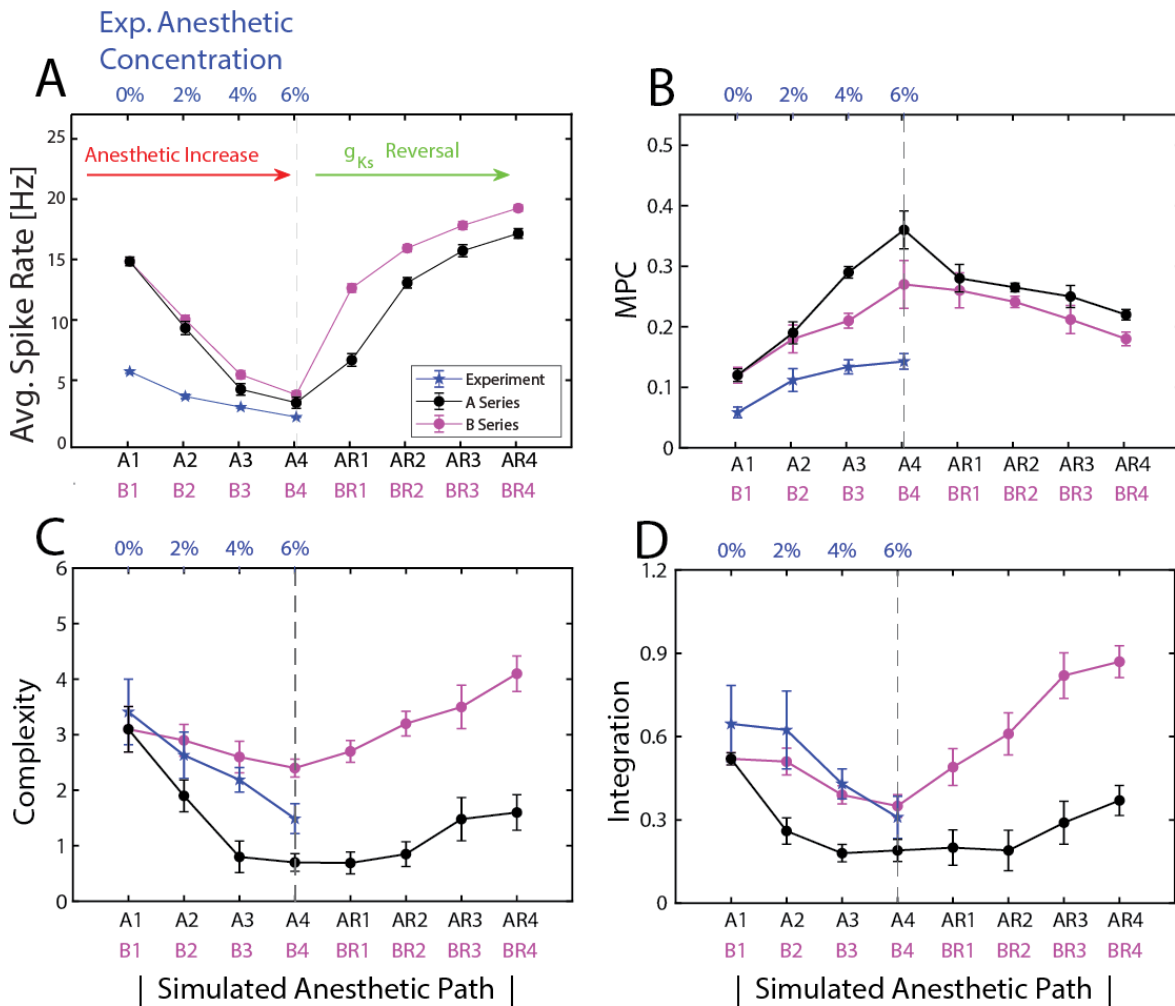
339

341 **Fig 4. Characterization of anesthetic effects on network dynamics and their**
342 **simulated ACh reversal.** Measures of network dynamics computed from experimental
343 data and optimized model networks as a function of anesthetic concentration and
344 simulated reversal level: **A)** Average spike rate **B)**. Mean Phase coherence **C)** Complexity
345 C(X) **D)** Integration I(X). A1-AR4/B1-BR4 (x-axis) denote simulated anesthetic
346 concentration levels and reversal states obtained in optimized networks with
347 corresponding parameters listed in **Table 2**. Black line denotes simulations with A-series
348 parameter sets (g_{Ks} constant) and pink line denotes simulations with B-series parameter
349 sets (changing g_{Ks}). Blue line (with corresponding axis labels on the top) denotes
350 measures computed from experimental spiking data at different desflurane
351 concentrations. All calculations were made for 6s intervals and then averaged over 5
352 intervals. Error bars are +/-SEM.

353 These four measures, average spike rate, MPC, I(X) and C(X), were used in the

354 evolutionary algorithm to optimize the fit of synaptic parameters to the experimental data

355 (see Methods section). In the next section, we validate our optimized networks by

356 comparing additional measures of network connectivity with the experimental data.

357

358 <u>Anesthetic and reversal effects on Network Connectivity</u>

359 We estimated network excitatory and inhibitory synaptic strengths, as well as network

360 excitatory and inhibitory connection probabilities, in the optimized networks and

361 compared them directly to these same measures computed from the experimental data.

362 These excitatory and inhibitory network connectivity measures were computed using

363 cross correlogram analysis as described in the Methods section (Fig 10) and based on

364 previous works [23].

365

366 The optimized networks displayed similar decreases in the strength of excitatory network

367 connectivity with increased levels of anesthetic as observed in the experimental data (Fig

368 5A). Both the A-series and B-series results followed similar trajectories, with the A-series

369 results reporting somewhat smaller excitatory connectivity strength values. This is due to

370 the fact that the evolutionary algorithm returned significantly lower NMDA efficacy for the

371 A-series, compared to the B-series. On the other hand, excitatory network connectivity

372 probability is very similar for both parameter series as the structural connectivitiy density

373 of excitatory synapses is the same in all model networks (see Methods section).
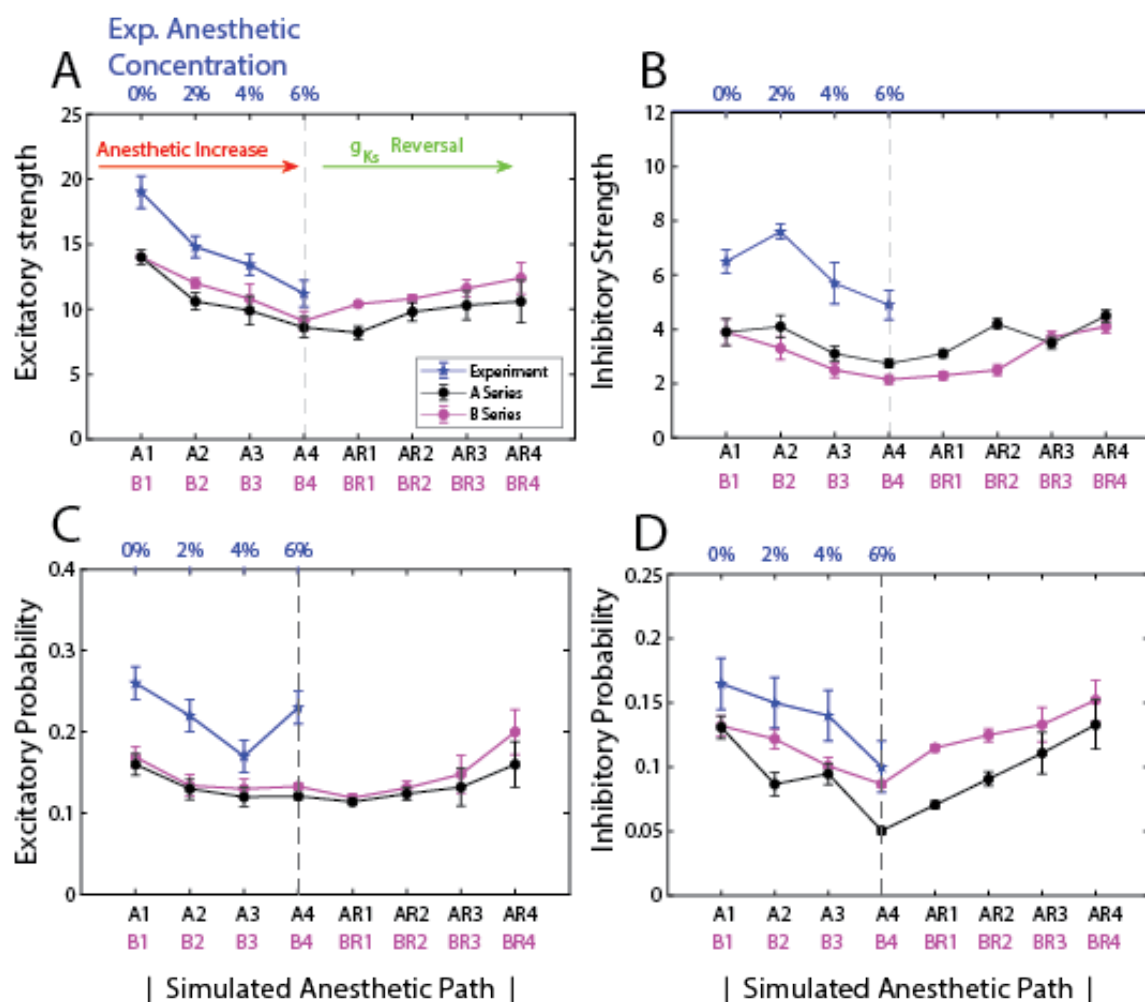
374

375

376

Fig 5. Characterization of anesthetic effects on network connectivity and their simulated ACh reversal. Measures of network connectivity computed from experimental data and optimized model networks as a function of anesthetic concentration and simulated reversal level: **A)** network excitatory connectivity strength, **B)** network inhibitory connectivity strength, **C)** network excitatory connectivity probability, **D)** network inhibitory connectivity probability. A1-AR4/B1-BR4 (x-axis) denote simulated anesthetic concentration levels and reversal states obtained in optimized networks with corresponding parameters listed in **Table 2**. Blue line (with corresponding axis labels on the top) denotes measures computed from experimental data, black (pink) line denotes measures computed from A-series (B-series) network simulations. In these measures, the presence of a significant connection was determined through cross correlogram analysis as described in Methods section. Error bars of +/-SEM.

392   The experimental data, as well as simulation results for both the A and B series networks,

393   showed decreases in inhibitory network connectivity strength and probability as a function

394   of anesthetic concentration. This seems a counterintuitive result since $GABA_A$ synaptic

395   efficacies increase with desflurane level, and were explicitly modeled as such in our

396   networks. However, this result may be a consequence of decreases in excitatory network

397   synaptic strength and connectivity probability. Namely, inhibitory cells receive less

398   excitatory drive, subsequently firing fewer spikes and, thus, limiting their effect on

399   postsynaptic targets.

400

401   Additionally, we observed that the strength of network inhibitory connectivity in the A-

402   series networks was generally stronger than in the B-series networks. This observation

403   agrees with the fact that the $GABA_A$ conductance is higher in the A-series parameters

404   than in the B-series. Counterintuitively, network inhibitory connectivity probability was

405   lower and more variable in the A-series networks compared to the B-series networks.

406

407   <u>Effects of ACh-induced anesthetic reversal on network functional connectivity</u>

408   The results discussed above report trends observed for measures of average network

409   activity, such as frequency, mean phase coherence, integration and complexity, as well

410   as network connectivity strength and probability. And while ACh-induced reversal

411   reinstated these network-level measures, the measures do not account for recovery of

412   functional connectivity in the network which would contribute to information processing.

413   In this section, we investigate how ACh reversal affects the relative frequency profile of

414   individual neurons with respect to other neurons in the network and also look at effects of

415   reversal on the cellular-level functional connectivity. These measures specifically assess

416   whether the internal dynamic structure of network activity is reinstated during the ACh

417   reversal.

418

419   To accomplish this, we first compared the firing rate of each neuron (or unit) in the

420   experimental data and in the optimized networks at each level of anesthetic concentration

421   to its firing rate in the waking state (Fig 6 and S1 Fig). In the figure panels, the x-axis

422   represents firing frequency of individual cells for different anesthetic levels and the y-axis

423   represents the firing frequency for the same cells in the non-anesthetic (0% or A1/B1)

424   conditions. For the experimental data mutliple units can be potentially detected on a single

425   electrode. This led to potential ambiguity in neurons assigned across anesthetic levels.

426   To address the, neuron identity was based on firing rate in the 0% case. Namely, for units

427   recorded on each electrode, the fastest firing units for 0% anesthesia were given the

428   same ID as the fastest firing units in the 6% case. The results showing an overall linear

429   relationship (Fig 6 and S1 Fig) indicates preservation of relative frequency ordering

430   between the neurons. Deflection of the slope of the linear relationship towards vertical

431   indicates the decrease in absolute firing frequency observed for different anesthetic

432   levels.

433

434   We observed that, generally, in both experiments and simulation results the relative

435   frequency of the neurons was preserved, i.e. neurons that fired at higher frequencies as

436   compared to other cells in non-anesthetic conditions retained higher firing frequencies at

437   the different anesthetic levels, albeit absolute frequencies decreased. Conversely,

438 neurons that maintained lower firing frequencies (relative to other cells) in the non-

439 anesthetic state continued firing at lower relative frequencies in the anesthetic conditions.

440 Qualitatively similar results were observed for A-series networks (Fig 6) and B-series

441 networks (S1 Fig).

442

443 Importantly, during the simulated ACh-induced reversal (AR-series in Fig 6C; BR-series

444 in S1 Fig), the relative relationship between firing frequencies of neurons remained the

445 same, with individual cell frequencies increasing back towards their non-anesthetic values

446 as evidenced by the slope of the linear relationship for higher reversal states tending

447 towards one. This result suggests that individual cells return to roughly the same firing

448 rates during ACh-induced reversal as they exhibited in the simulated waking state.

449

450 To explore detailed changes in cellular-level functional connectivity in the optimized

451 networks, we created functional adjacency matrices from the estimated pairwise

452 excitatory connectivity strengths at all simulated anesthetic and reversal conditions,

453 measured via identification of the peak/trough of the spiking cross correlogram as

454 described in the Methods section. We then calculated the cosine similarities between the

455 created functional adjacency matrices obtained for each anesthetic and reversal level (Fig

456 7). A cosine similarity of 1 indicates that the functional adjacency matrices are identical,

457 whereas cosine similarity of zero indicates that they are uncorrelated.

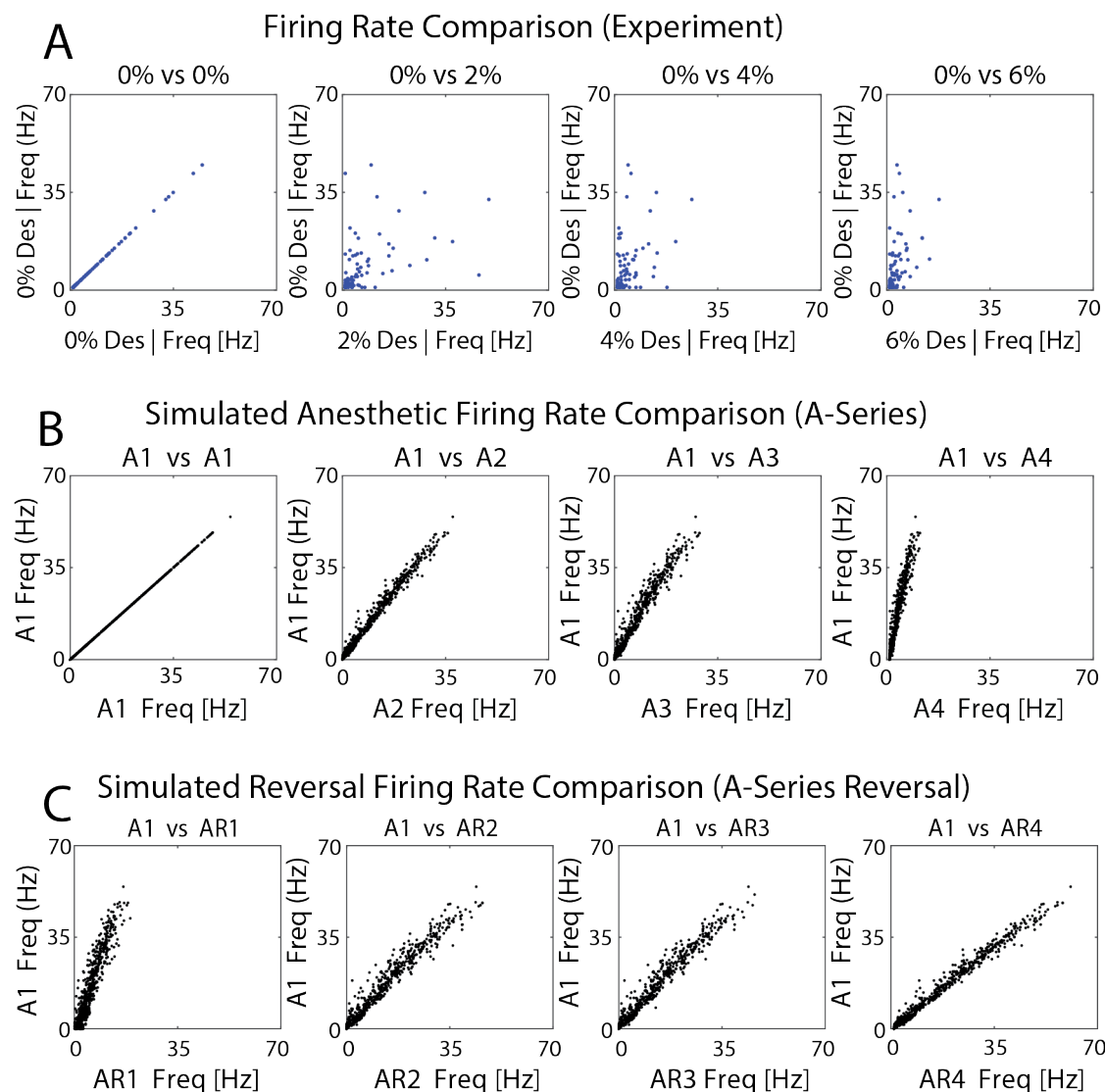**Fig 6. Effects of anesthetic concentration and simulated ACh-induced reversal on relative profiles of neuronal firing frequency.** Each panel depicts the firing frequency of each neuron in a given anesthetic/reversal state (x-axis) compared to its firing frequency in the non-anesthetic condition (0% desflurane or A1) (y-axis) A) Units recorded in the experimental data; B,C) Neurons in A series optimized networks and reversal.

469   The analysis was performed on all measured excitatory connections (Fig 7B, D)

470   independently of whether their strengths passed the significance test, and separately,

471   considering only connections that were deemed significant (thresholded, all other

472   connections were set to zero, Fig 7A, C).

473

474   We observed that the functional adjacency matrices became less correlated with each

475   other with increasing anesthetic levels. However, ACh reversal resulted in a significant

476   increase in the correlation between the baseline non-anesthetic adjacency matrix (A1 or

477   B1) and the fully reversed functional adjacency matrix (AR4 and BR4). This trend was

478   observed when all connections were considered as well as when only significant

479   (thresholded) connections were included, indicating that the cellular-level dynamic activity

480   structure was largely recovered with ACh-induced reversal.

481

482   In summary, our model results showed that multiple measures of network connectivity

483   (Figs 5 and 7) increased with ACh-induced simulated reversal suggesting that increases

484   in cellular excitability, mediated by muscarinic effects of ACh, can reinstate network

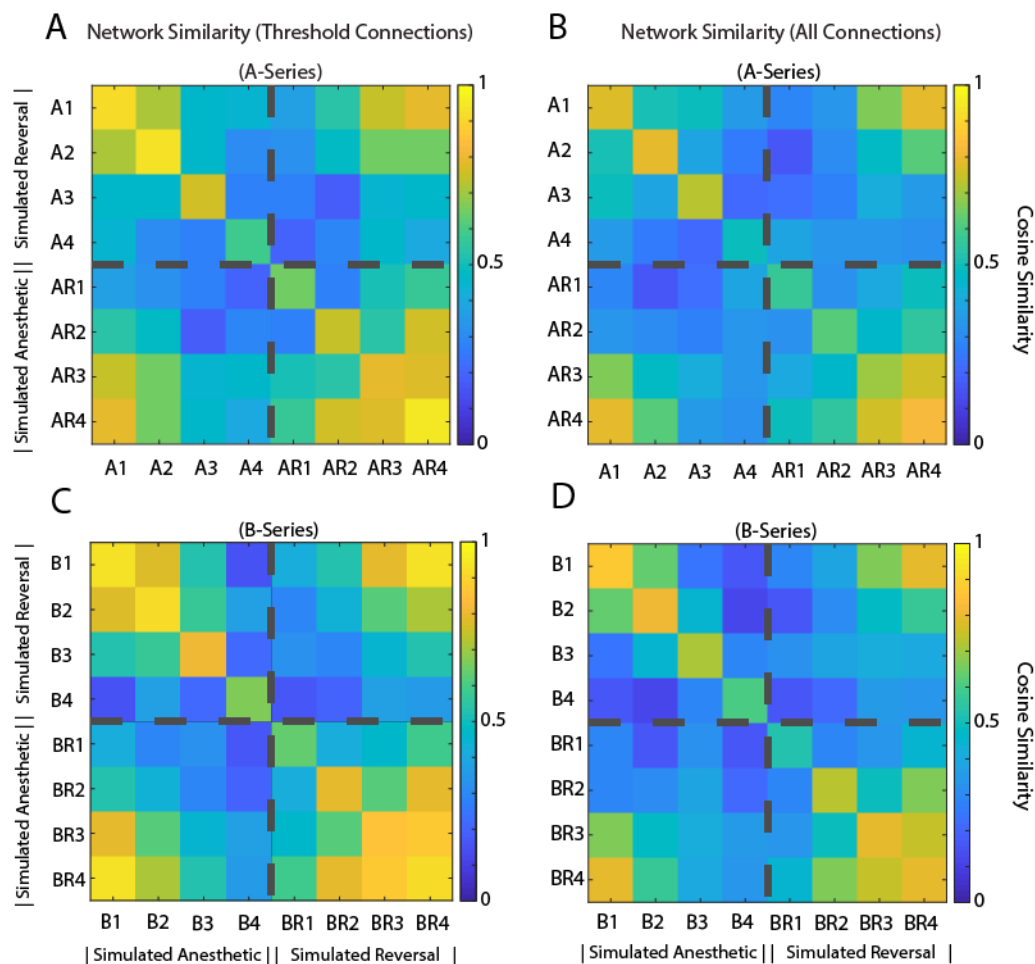485   dynamics dictated by synaptic connectivity.

486

Fig 7. Effects of anesthetic concentration and ACh-induced reversal on the similarity between cellular functional connectivity. Cosine similarity was computed for every pairwise combination of cellular functional connectivity matrices obtained for different simulated anesthetic level (A, B - series) and reversal state (AR, BR -series). **A-D**) Cosine similarities of functional connectivity matrices consisting of (A, C) only significant (as detailed in the Methods section) connections and (B, D) all connections in A- and B-series network simulations. Increased similarity between AR4 and A1 (and BR4 and B1) shows reinstatement of functional connectivity that was degraded with simulated anesthetic concentrations.

501   **Discussion**

502   The goal of this investigation was to simulate the multisynaptic effects of an anesthetic

503   and the modulating effect of muscarinic ACh receptor activation in a neuronal network

504   model. We first examined if excitatory and inhibitory synaptic changes typically produced

505   by the inhalational anesthetic desflurane led to neural network behavior similar to

506   experimentally observed neuron activity as characterized by various measures including

507   population firing rate, phase coherence, monosynaptic spike transmission, and the

508   information theoretic measures integration and complexity. Second, we investigated if an

509   exogenously induced increase in the level of ACh acting on muscarinic receptors could

510   reverse the effect of the anesthetic as suggested by prior behavioral experiments.

511

512   Simulation of the anesthetic effect

513   We simulated the effect of anesthetic desflurane on the neuronal network by reducing the

514   response of excitatory synapses and facilitating that of inhibitory synapses. General

515   anesthetics commonly potentiate GABAergic synaptic receptor transmission through

516   modification of inhibitory post synaptic potential (IPSP) amplitude and duration, as well

517   as through inhibition of glutamatergic receptor excitatory post synaptic potential (EPSP)

518   amplitude and duration. The relative strength of these effects depends on the class of

519   anesthetic [4,20]. Desflurane inhibits binding at NMDA receptors while potentiating

520   postsynaptic inhibition at GABA$_A$ receptors. Some anesthetics, but not desflurane, also

521   suppress AMPA receptors. The effect of anesthetics on nicotinic and muscarinic

522   receptors is more diverse. Some anesthetics also modify the activity of cholinergic

523   neurons projecting to the cortex [17]. Regarding its electrophysiological effects,

524 desflurane has been shown to decrease average spike rate, excitatory and inhibitory
525 monosynaptic transmission, and population measures of neuronal interactions in the
526 cortex [8,24]. These changes in neuronal activity observed *in vivo* have not been directly
527 linked to the corresponding synaptic effects observed *in vitro*.

528

529 In our study we found that potentiation of inhibitory GABAergic and inhibition of excitatory
530 glutamatergic NMDA synaptic receptors do indeed lead to graded decreases in
531 population activity and increases in synchronization, as quantified by firing rate and mean
532 phase coherence, as well as measured decreases in integration and complexity.
533 Additionally, we were able to recover changes in functional network connectivity which
534 matched changes seen in literature [25,26]. The simulation results were robust; although
535 some of the measures (frequency, MPC, I(X) and C(X)) were used for optimization of
536 model parameters via the differential evolution algorithm, the results held for a wide range
537 of non-fitted measures within physiologically reasonable limits. Moreover, the parameter
538 fits obtained for increasing levels of anesthetic matched in their relative magnitudes to the
539 reported anesthetic induced changes in synaptic efficacy.

540

541 Understanding the mechanism of anesthesia through computational modeling
542 The cellular mechanism of anesthetic action with respect to loss of awareness has been
543 a subject of intense investigation. Computational models are actively used to make
544 progress in this area of research. Because differing classes of anesthetics elicit different
545 effects on synaptic receptor subtypes, many modeling approaches aim to determine how
546 nuanced changes in receptor binding and synaptic activity lead to changes in neural or

547   electroencephalographic activity. For example, in mean field models, GABAergic and

548   glutamatergic synaptic changes are attributed to a single parameter that maps to different

549   concentrations of general anesthesia [27]. Other modelling approaches seek to

550   understand the mechanism of specific anesthetic agents; for example, the effects of

551   propofol have been studied through the modeling of both $GABA_A$ and $GABA_B$

552   amplitude/duration and the effects on cortical synchrony and EEG rhythms [18,28].

553   Enflurane and isoflurane are other commonly modeled anesthetics where the roles of

554   both glutamatergic receptor binding and GABAergic effects are taken into consideration

555   [28–30]. Anesthetic action effected through post synaptic potential (PSP) changes, from

556   a modelling perspective, is a relativity robust explanation supported by its effectiveness

557   across modelling paradigms. These include "mean field" models as well as networks of

558   "integrate and fire", "Izhikevich "and "HH" neurons, which all show reduced activity and

559   changes to population synchrony when modeling anesthetic effects on synaptic receptors

560   [30–32].

561

562   Our study is distinguished from former computational models of anesthetic effects by the

563   independent consideration of the effects on $NMDA_R$ and $GABA_R$ through PSP changes,

564   as well as of cholinergic influence through changes in the muscarinic M-current. We also

565   used a more biologically realistic log-normal distribution for synaptic weights [33].

566   Because we had access to experimental spike data, we were able to directly fit our model

567   to empirical data at graded levels of anesthesia and then test our hypothesis regarding

568   cholinergic anesthesia reversal.

569

570

571   <u>Anesthetic effects on spike synchrony</u>

572   A common brain signature of general anesthesia is the loss of global functional

573   connectivity between specialized regions of the cortex while local populations show

574   increases in neural synchrony [25,34,35]. Cellular and network mechanisms leading to

575   neural synchrony have been studied extensively in the field of computational

576   neuroscience [36–38]. A set of possible network wide mechanisms are the PING

577   (pyramidal interneuron network gamma) class of mechanisms, where stable,

578   synchronous activity patterns emerge when inhibition periodically shuts down excitation

579   in the network [39–43]. The propensity of neural network synchrony can also depend on

580   intrinsic cellular excitability properties, an example being changes from Type 1 to Type 2

581   membrane excitability. Type 1 and Type 2 neural excitability describe the well-

582   characterized differences in spike generation dynamics that can occur generally between

583   different types of neurons, and can occur in the same neuron under different

584   pharmacological conditions, such as changing ACh levels. Type 2 dynamics originate

585   from increased competition between depolarizing and hyperpolarizing currents as

586   compared to Type 1 [44]. These differences exemplify themselves in the onset and

587   steepness of firing frequency-input (i-f) curves and the shape of phase response curves

588   (PRCs) which in turn determine synchronizability of the networks. Neurons exhibiting

589   Type 1 excitability respond more rapidly with higher firing frequency changes to changing

590   stimulus magnitude as compared to Type 2 cells, and also decreased propensity to

591   synchronize stemming from the shape of their PRC curves [21,45,46].

592

593   Thus, as also discussed below, ACh can play a double edged role in affecting network

594   synchrony. On one hand, decreasing levels of ACh during increased anesthesia levels

595   can promote synchrony, as it has been shown that activation of the K+ M-current

596   mediates the transition from Type 1 to Type 2 membrane excitability [43], while on the

597   other hand, the increase of ACh-mediated effects during reversal can offset the

598   decreasing synaptic efficacies with higher cellular responses (increasing steepness of i-f

599   curve). In our modelling results on ACh mediated reversal, we show that we can evoke

600   a transition between high frequency asynchronous population behavior to low frequency

601   synchronous activity via both mechanisms: by potentiation of IPSP and inhibition of

602   EPSP, and ACh-mediated modulation of cell excitability. This demonstrates that it is

603   possible for the population synchronization observed in response to anesthesia to

604   develop in response to changes in psp alone or to concurrently active cellular

605   mechanisms.

606

607   Predicting anesthesia reversal by ACh

608 Prior experimental studies demonstrated that the behavioral expression of the anesthetic

609   state can be reversed by stimulating the cholinergic system of the brain by various means

610   *in vivo* and *in vitro* in both humans and animals [15,17,18,47]. To date, no modelling study

611   has attempted to simulate the reversal of neuronal effects of anesthesia by modulating

612   the interaction between cholinergic and other synaptic effects. In this work we

613   demonstrated that ACh acting via blocking the muscarinic slow potassium current can

614   reverse the general anesthetic effect on spiking dynamics and population activity, via

615   mechanisms described above. Specifically, we showed that decreasing the influence of

616   the M-current under simulated anesthesia leads to an increase in firing rate and neural

617   interaction measures, showing a population wide reversal of anesthesia-induced synaptic

618   changes. This finding suggests a possible cellular mechanism for the induced reversal of

619   anesthesia effects on PSPs consistent with experimental studies [11,16].

620

621   To simulate the overall effect of elevated ACh in the network, we chose to alter the

622   muscarinic receptor-mediated pathway. The role of muscarinic ACh receptors in affecting

623   the state of the animal depends largely on the type of general anesthetic used. Desflurane

624   exerts a nonlinear effect on muscarinic ACh receptor activation in a concentration-

625   dependent manner [7]. We also showed that the addition of decreasing acetylcholine

626   influence via the muscarinic pathway during anesthesia (B series) leads to similar reversal

627   endpoints to those with altering NMDA and GABA synaptic changes alone (A series).

628   The choice to model changes in anesthetic ACh influence (B series) in addition to synaptic

629   changes alone (A series) was made to generalize the effects of common inhalational

630   anesthestics which can affect both the cholinergic as well as the glutamatergic and

631   GABAergic pathways (Fig 1). By considering solely the effect of changes on IPSPs via

632    $GABA_R$ and EPSPs through $NMDA_R$ we show that not only can changes in population

633   activity (firing rate, synchronization and entropy), be accomplished without changes in

634   cholinergic influence but that increasing cholinergic influence alone can reverse these

635   effects. This demonstrates that cortical cholinergic presence has the potential to mitigate

636   the general effects of inhalational anesthesia. In many cases, however, such as for the

637   effects of desflurane, inhalational anesthesia can affect muscarinic and nicotinic ACh

638   receptor binding and for this reason we decided to model the cooperative effects from

639   changes in synaptic EPSP/IPSP and cellular excitability changes via the M-current. In the

640   case of cholinergic reversal, however, this confounded the role of ACh, as the changes

641   in ACh due to anesthesia could be argued to be trivially reversed in the reversal states.

642

643   In this study, we used measures of synaptic functional connectivity, computed from

644   average pairwise correlations of neuron spiking, to quantify changes in overall network

645   behavior in both anesthesia and reversal conditions. We showed that the cosine similarity

646   in the functional connectivity matrix increased for the full reversal state when compared

647   to the high anesthetic state. This means that specific neuron to neuron functional

648   connectivity was highly correlated between the awake and reversal states but not the

649   anesthesia states. This suggests that the functional topology of a network can be

650   reversed through a different receptor pathway than is used to achieve the state of

651   anesthesia. Likewise, the population measures of integration and complexity were

652   increased by the cholinergic decrease in M-current. In fact, prior experimental studies

653   showed that muscarinic receptor activation could reverse isoflurane-induced changes in

654   electroencephalogram cross entropy [16]– a quantity related to brain functional

655   complexity presumed to be associated with the conscious state [16,48].

656

657   In the past, anesthesia reversal has been achieved by a variety of drugs and methods of

658   administration in experimental studies. For example, microinjection of nicotine into the

659   thalamus led to the recovery of the righting reflex in rodents anesthetized by sevoflurane

660   [15], and a similar reversal from isoflurane was observed in response to microinjection of

661   histamine into the basal forebrain [49]. Unlike general anesthesia, however, the

662   mechanisms for induced reversal may be specific to the type of anesthetic agent used.

663   An example of this can be seen when comparing the effects of the $GABA_A$ antagonist,

664   gabazine, on the effects of propofol as well as ketamine [50]. The application of gabazine

665   led to wake-like responses when rats were sedated with propofol, which acts through

666   potentiation of $GABA_A$ receptors, but gabazine was ineffective when used during

667   administration of ketamine, which has been known to act through modulation of NMDA

668   receptors. These previous studies suggest that the phenomena of induced reversal can

669   be demonstrated in controlled rodent studies, but a similar effect has been suggested in

670   human studies [51]. Another example is the clinical case where a patient's use of Ritalin,

671   a central nervous system stimulant, required an increase of general anesthetic dose for

672   sedation [52]. In rodents, Ritalin was found to cause emergence from sedation induced

673   by isoflurane [53].

674

675   Our results predicting cholinergic recovery of neuronal population dynamics, inter-

676   neuronal functional connectivity and complexity lends support to the evidence that the

677   brain state altered by anesthesia is at least partially reversible. In clinical use, the effects

678   of anesthesia can linger after the drug is no longer administered [54]. For this reason,

679   there are both translational and phenomenological motivations to investigate induced

680   recovery from anesthesia. Our study gives insight into the synaptic and network

681   mechanisms by which central nervous system changes caused by anesthesia can be

682   mitigated by the administration of a functional agonist.

683

684

685

686 <u>Limitations and directions for future work</u>

687 We recognize a few limitations of this study. First, our model was based on random

688 connectivity between E and I cells instead of on a detailed representation of a specific

689 neural circuit. Other modeling studies included thalamocortical interactions [55,56] or a

690 cortical macro structure aimed at understanding how a multilayer architecture can

691 influence the effects of anesthesia-induced changes in synaptic strength [55,57–59]. We

692 argue that, for a first approximation, a generic random model is sufficient because little is

693 known about the identity of brain regions that are responsible for mediating the anesthetic

694 action, particularly with respect to the suppression of consciousness. We compared our

695 model predictions to data obtained from visual cortex, which may not be the primary site

696 of anesthetic action to suppress consciousness. It can be argued, however, that the

697 experimentally observed changes in neural firing rates, coherence, connectivity,

698 complexity, and other related measures are probably sufficiently general to describe the

699 mechanism of synaptically induced network effects we intend to understand. Of course,

700 to understand the full effect of anesthesia on the observed behavior of a live animal may

701 require the modeling of additional effects in multiple brain regions including widespread

702 cortical areas, thalamus, subcortical and brainstem arousal centers, to mention a few.

703 Although other models of anesthetic mechanism have incorporated thalamocortical

704 interactions [55,58], none have simulated anesthetic reversal and still fall short of

705 modeling corresponding behavioral effects. Additionally, general anesthetics have

706 secondary effects on voltage-gated and ligand-gated channels, two-pore potassium

707 channels, and other targets that were not represented in our model [4,7,20]. Inclusion of

708   these additional effects could provide a more nuanced simulation with potentially closer

709   fit to experimental data. Despite the missing details, the success of our simulations

710   suggests that our model likely captured the essential mechanistic elements of anesthetic

711   action and its reversal.

712

713   Conclusion

714   In summary, we demonstrated that experimentally observed changes in neural activity

715   and functional connectivity caused by desflurane could be computationally reproduced by

716   modulating synaptic efficacy according to the known synaptic effects of the anesthetic.

717   Additionally, we showed that by modulating the M-current alone, the effect of anesthesia

718   on neural activity and functional connectivity in the network could be at least partially

719   reversed. In the future, more comprehensive models that take into account cortical

720   architecture, thalamocortical interactions and a broader array of cellular mechanisms will

721   help to fully understand the complex roles of synaptic modulation in producing the

722   observed neuronal network and behavioral effects of anesthesia.

723

724   **Methods**

725   Experimental Data

726   Experimental results were based on the analysis of data collected in previous studies;

727   for an in depth description refer to the original study [60]. Briefly, rats were surgically

728   implanted with a multishank, 64 contact microelectrode array in the visual cortex (V1).

729   After a post-surgery recovery period, they were placed in a cylindrical anesthesia

730   chamber for administration of inhalation anesthetic. Desflurane was applied in the

731   sequence of 8, 6, 4, 2, and 0% inhaled concentrations for 45 to 50 min at each level.

732   Neural activity was recorded during the duration of the experiment and subsequently

733   processed to extract multiunit spiking information. For this study, we analyzed unit spiking

734   activity collected during the 0, 2, 4 and 6% desflurane exposure sessions.

735

736   <u>Neuron Modeling</u>

737   Excitatory and inhibitory neurons are modeled using the Hodgkin-Huxley formalism [61]

738   with parameters selected based on a model that emulated properties of both cortical

739   pyramidal neurons and inhibitory interneurons [62,63]. The neuron model contained

740   sodium, delayed rectifier potassium, slow M-Type potassium and leak currents as

741   described in the following equations:

742

743
$$\frac{dV}{dt} = -g_{Na}m_\infty^3 h(V - E_{Na}) - g_{Kd}n^4(V - E_k)$$

746
$$-g_{Ks}z(V - E_k) - g_L(V - E_L) + I_{noise} - I_{syn} + I_{DC} \tag{1}$$

744
$$\frac{dX}{dt} = \frac{X_\infty(V) - X}{\tau_X(V)} \; for \; x = \{h, n, z\} \tag{2}$$

745
$$m_\infty(V) = \frac{1}{1 + e^{\left(\frac{-V - 30}{9.5}\right)}} \tag{3}$$

747
$$h_\infty(V) = \frac{1}{1 + e^{\left(\frac{V + 53}{7.0}\right)}} \tag{4}$$

748
$$n_\infty(V) = \frac{1}{1 + e^{\left(-\frac{V + 30}{10}\right)}} \tag{5}$$

749
$$z_\infty(V) = \frac{1}{1 + e^{\left(-\frac{V + 39}{5.0}\right)}} \tag{6}$$

750
$$\tau_h(V) = 0.37 + \frac{2.78}{1 + e^{\left(\frac{V + 40.5}{5.0}\right)}} \tag{7}$$

751
$$\tau_n(V) = 0.37 + \frac{1.85}{1 + e^{\left(\frac{V+27}{15}\right)}} \tag{8}$$

752
$$\tau_z(V) = 75 \tag{9}$$

753

754 In the above, V is the membrane voltage while m, n, h and z represent the unitless gating

755 variables of the ionic current conductances. I_{syn} is the synaptic current input to the cell

756 from other neurons in the network and has units of $\mu A/cm^2$. I_{noise} is a noise input consisting

757 of randomly occurring brief current pulses with average frequency of 0.1 Hz, a duration

758 of 2 ms and strength of 4 $\mu A/cm^2$. This noise input was sufficiently strong to generate an

759 action potential in the absence of any other inputs. I_{DC} is a biasing constant current input

760 of -0.77 $\mu A/cm^2$. E_{Na}, E_K and E_L are the reversal potentials for sodium, potassium, and

761 leak currents, respectively, set to E_{Na} = 55 mV, E_K = −90 mV, E_L = −60 mV.

762 This neuron model, with the slow M-type K+ current, was developed to model the

763 muscarinic-receptor effects of acetylcholine in cortical pyramidal neurons [44]. The

764 properties of this neuron model when g_{Ks} = 0 mS/cm^2 describe a neuron under high levels

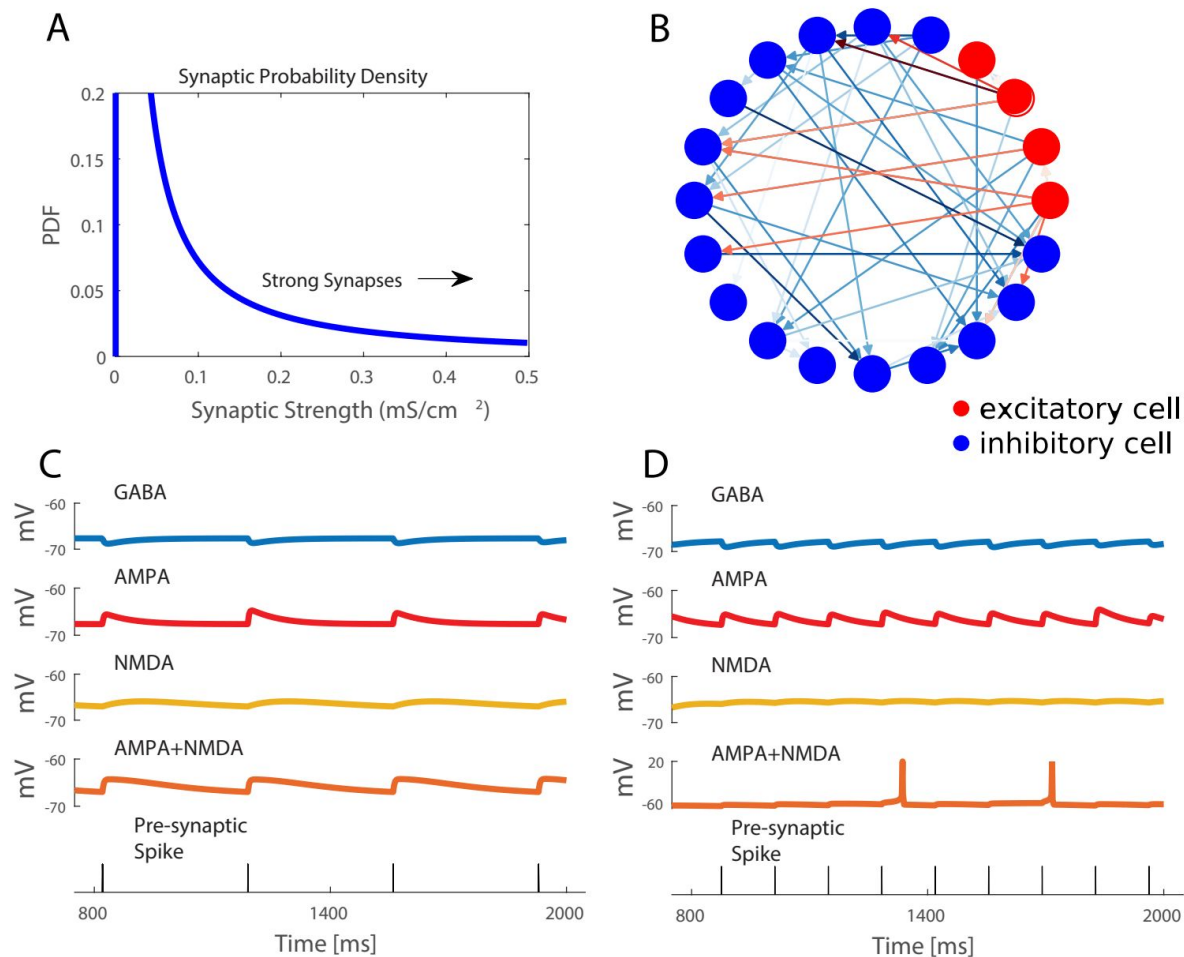765 of acetylcholine while g_{Ks} = 1.5 mS/cm^2 represents a low acetylcholine state.

766

Fig 8. Network structure is populated by lognormal distributed random connection strengths A) Synaptic strengths in model networks varied according to a lognormal distribution with a minority of connections being mediated by strong synaptic strengths, while weak synaptic strengths constitute majority of connections **B)** Simulated network consists of 200 inhibitory and 800 excitatory cells connected randomly with 10% probability. Connection color reflects the log of synaptic strength. **C, D)** Postsynaptic potential time courses in response to synaptic currents mediated by different receptors. Excitatory currents are modeled with both AMPA and NMDA mediated currents. Bottom panel shows timing of presynaptic spikes, for simplicity both inhibitory and excitatory presynaptic neurons are shown with the same spike times.

777

778

779

780

781   <u>Network Design</u>

782   We constructed E-I networks with 800 excitatory and 200 inhibitory neurons (Fig 8B).

783   Neurons were connected randomly with 10% probability. Synaptic strengths followed a

784   log normal distribution, as suggested to occur in cortical networks (Fig 8A) [33] .The

785   distribution was defined by parameters $\mu = -20.0, \theta = 9.4$, and characterized by the

786   equation:

787
$$PDF_{Log}(X) = \frac{1}{x\theta\sqrt{2\pi}} \left(e^{-\frac{(\ln x - u)^2}{2\theta^2}} \right) \qquad (10)$$

788

789   μ and θ are defined such that they are the mean and standard deviation of the logarithm

790   of x if the logarithm of x was normally distributed. This connectivity distribution was chosen

791   such that ~0.2% of excitatory connections would elicit an action potential in a post-

792   synaptic cell in the absence of other inputs for our parameter values representing the

793   wake state. The value of 0.2% was determined by experimental data in which cross

794   correlogram analysis showed a 0.2% "strong" connection probability among a local

795   population of neurons [8].

796

797   Synaptic currents mediated by AMPA, NMDA and GABA$_A$ receptors were included in the

798   network such that excitatory synaptic currents were given by $I_{exc} = I_{AMPA} + I_{NMDA}$ and

799   inhibitory synaptic currents by $I_{inh} = I_{GABA}$. All synaptic currents were modeled with a

800   double exponential function of the form

801
$$I_X = P_x \, B_x \, V_{0.5} \, g_{\log} \left(e^{-\frac{t-t_{spike}}{\tau_{Xs}}} - e^{-\frac{t-t_{spike}}{\tau_{Xf}}} \right) (V - E_{\mathrm{x}}) \tag{11}$$

802   where X indicates the receptor type (AMPA, NMDA or GABA_A), t_spike is the time of the

803   presynaptic spike and g_log is the synaptic conductance drawn from the lognormal

804   distribution. Reversal potential E_x was set at −75 mV for inhibitory synapses and 0 mV for

805   excitatory synapses. The term g_o will be used to refer to $B_x \, V_{0.5} \, g_{\log}$ .Time constants τ_{Xs}

806   and τ_{Xf} governed the fast rise and slow decay of the synaptic current and were set as

807   follows:

808
$$t_{\mathrm{AMPAf}} = t_{\mathrm{NMDAf}} = t_{\mathrm{GABA_Af}} = 0.2 \; ms \tag{12}$$

809
$$t_{\mathrm{AMPAs}} = 3.0 \; ms \, , t_{\mathrm{NMDAs}} = 200.0 \; ms, \; t_{\mathrm{GABA_As}} = 5.5 \; ms \tag{13}$$

810   The NMDA synaptic conductance was additionally gated by the post-synaptic voltage

811   [64,65] described by the additional pre-factor B_x:

812
$$B_{\mathrm{AMPA}} = B_{\mathrm{GABA_A}} = 1 \tag{14}$$

813
$$B_{\mathrm{NMDA}}(V) = \frac{1}{1 + e^{-\frac{V+10}{3.57}}} \tag{15}$$

814

815   Fig 8C, D illustrates time courses of the synaptic currents. Additionally, to account for

816   event-to-event variability, a variability pre-factor $V_{0.5}$, randomly chosen uniformly from

817   [0.5, 1], modulated the synaptic current induced by each pre-synaptic spike. Finally, the

818   scaling factors P_{x} simulated anesthetic effects on synaptic conductances. Values of P_{x} for

819   each receptor type were optimized to fit multiple measures of network dynamics for each

820   level of anesthesia. Values are listed in Tables 1 and 2 that show average parameter

821   values for optimizations performed on ten different network realizations, and the specific

822   parameter values used for the presented analysis of results, respectively.

823

824   <u>Measures and Metrics</u>

825   We use several different measures to quantify the changes between network states and

826   dynamics under different levels of anesthesia observed in the experimental data and

827   simulated in the neural network models.

828

829   *Integration and Interaction Complexity*

830   We computed the information theoretic measures Complexity C(X) and Integration I(X)

831   to quantify changes in the entropy of the network [22]. I(X) is a generalization of mutual

832   information that measures the amount of total entropy of a system that is accounted for

833   by the interactions among its elements. I(X) is zero when system elements are statistically

834   independent [22]. C(X) measures the total entropy loss due to interaction of system

835   elements, or, equivalently, the difference between the sum of the entropies of the

836   individual elements and the entropy of the entire system. C(X) is low for systems with

837   independent elements or with highly synchronous elements.

838   To compute these measures, the total spiking activity from an experimental recording or

839   a network simulation was partitioned into patterns by binning spike trains into 1 ms time

840   bins and constructing vectors for each time bin containing a 1 at the neuron index if the

841   neuron spiked within that time bin and a 0 if there was no spike (columns in Fig 9). The

842   set X of unique vectors, representing patterns of spiking activity within a bin, that occurred

843   across the data set were identified. Additionally, discretized spike vectors $X_i, i = 1, ..., N,$

844   were constructed for each cell (rows in Fig 9).

845

846   Integration was computed as

847 $$I(X) = \sum_{i=1}^{N} H(X_i) - H(X) \tag{16}$$

848

849   where $H(X_i) = -\sum_k p_k log p_k$ is the entropy based on the probability of a spike occurring

850   in the ith cell, and $H(X) = -\sum_j p_j log p_j$ is the entropy based on the probability of

851   occurrence of a spike pattern vector.

852   Complexity was computed as

853 $$C(X) = H(X) - \sum_{i=1}^{N} H(X_i|X - X_i) \tag{17}$$

854   Here, $H(X_i)$ is the entropy of the spike train belonging to neuron i while $H(X)$ is the entropy

855   of the set of spike vector for the entire interval. $H(X_i|X - X_i)$ is the conditional entropy

856   where X_i is the new spike vectors neglecting the ith unit and is conditioned on the spike

857   train of the ith unit. The metric is discussed greater detail in original study [22].
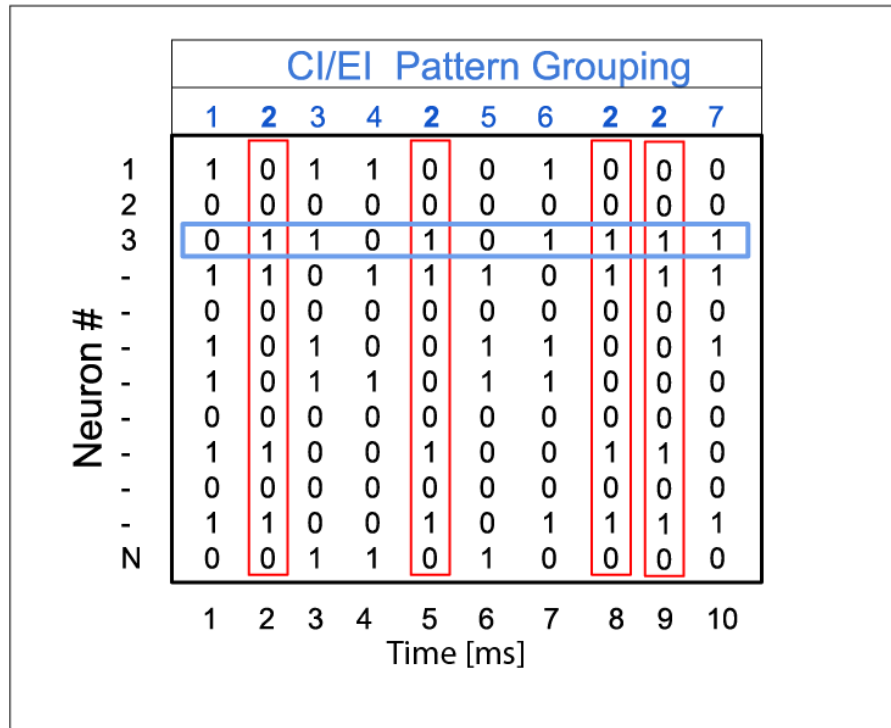
858

859

860

Fig 9. Binned spike patterns for complexity and integration measures. To compute entropy metrics complexity (C(X)) and integration (I(X)), spike trains were binned in 1 ms bins. H(X) in equation (16)/(17) is computed according to unique patterns associated with column vectors (red vectors) while H(X_i) is the entropy associated with a single neuron spike train (blue vector).

Mean Phase Coherence

We computed mean phase coherence to quantify the average phase relation between spike times of pairs of neurons in experimental recordings and network simulation. The pairwise mean phase coherence is given by

$$\sigma_{i,j} = \left| \frac{1}{N} \sum_{k=1}^{n} \left(\exp\left(i2\pi \frac{t_{j,k} - t_{i,k}}{t_{i,k+1} - t_{i,k}} \right) \right) \right| \qquad (18)$$

876

877 where $t_{j,k}$ is the time of the kth spike of the jth neuron and $t_{i,k}, t_{i+1,k}$ are times of

878 successive spikes of the ith neuron. Network mean phase coherence is the average of

879 $\sigma_{i,j}$ over all pairs of neurons.

880

881 For two neurons i and j, the mean phase coherence is 1 when the spike times of neuron

882 j always occur at the same relative phase in the cycle defined by two subsequent spikes

883 of neuron i. Conversely, pairwise mean phase coherence is zero when spikes of neuron

884 j occur at random phases of the neuron i spike cycle for the entire set of neurons i spike

885 times, due to averaging of phases.

886

887 *Functional connectivity probability and strength*

888 Functional connectivity probability and strength were determined through cross

889 correlogram analysis on spike trains [23] between pairs of neurons with minimum average

890 spike rate of 1 Hz. Since experimental recordings contained on average ~60 eligible units,

891 these measures for the simulated networks were computed based on spike trains of 60

892 eligible neurons. For each pair of cells, spike trains were segmented into 40 ms intervals

893 centered on each spike of the designated "reference" cell of the pair and discretized into

894 1.3 ms bins. Cross-correlations of discretized segments between the "reference" and

895 "comparison" cell for every "reference" cell spike were summed to form cross

896 correlograms (Fig 10).

897

898

899

900

901
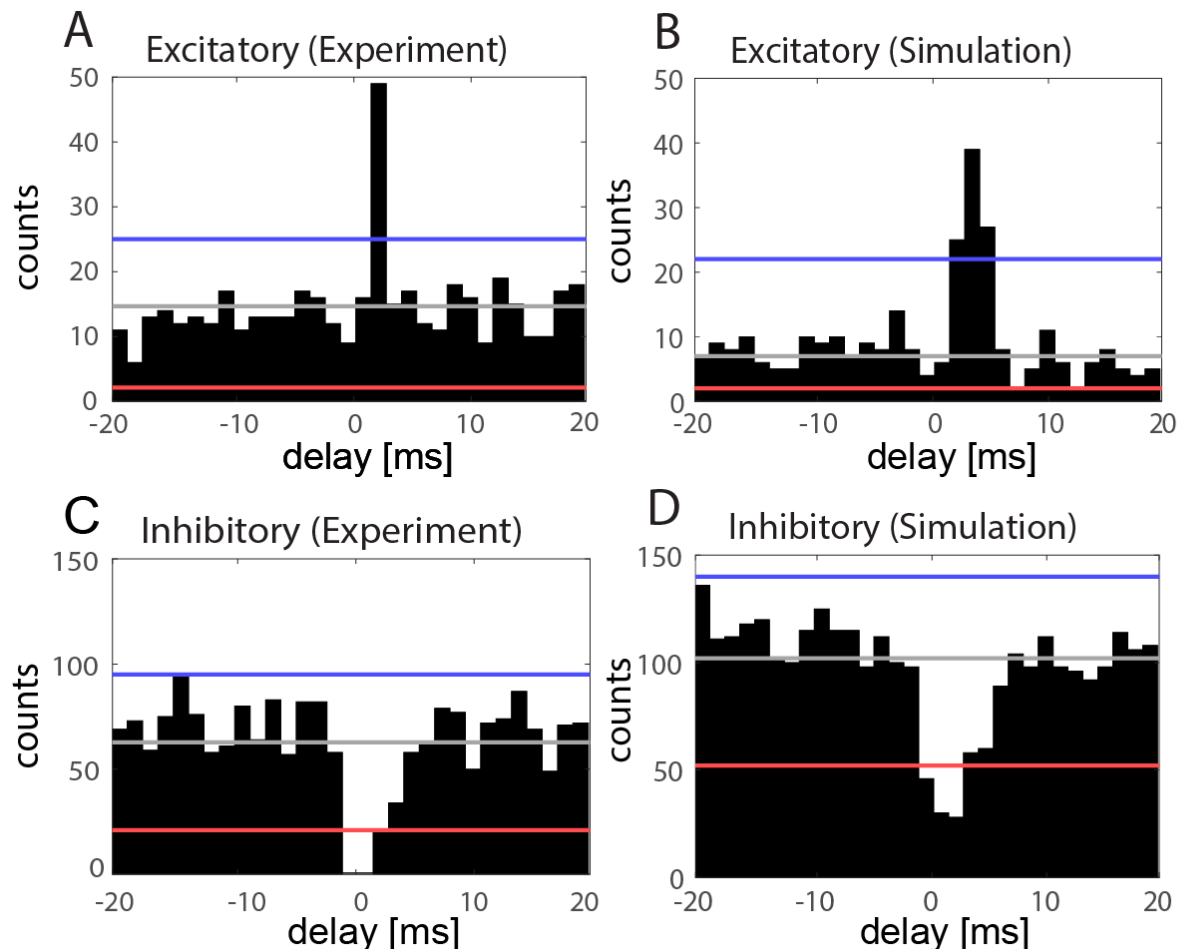
Fig 10. Cross Correlogram computes coincident spike relations by summing relative spike times of reference and comparison neurons A-D) Cross correlograms between example pairs of "reference" and "comparison" cells, centered at spike times of the "reference" cell, from the experimental recordings (left column) and simulated networks (right column). Significance bands were computed from a jittered data set of "comparison" cell spike times (gray line = mean of jittered data set, red line = excitatory significance, blue line = inhibitory significance, see text). **A-B)** Example cross correlograms showing significant excitatory connections between cell pairs. **C, D)** Example cross correlograms showing significant inhibitory connections between cell pairs.

912

913

914   Significance of correlations was determined by comparison to a constructed "jittered"

915   dataset. The jittered data set was formed by randomly "jittering" spike times of the

916   "comparison" cell by [-5,5] ms and then computing the cross correlogram. This was

917   repeated by 100 times to for the jittered data set. The global confidence band for

918   excitatory (inhibitory) connectivity was computed by taking the 97% confidence interval

919   associated with the global peak (trough) of the jittered data set. A significant connection

920   was determined when the peak (trough) of the original cross correlogram was greater

921   (less) than 2 times the 97% confidence interval when measured from the mean (blue/red)

922   [23].

923

924   Excitatory connectivity strength was determined by taking the difference in the peak

925   height withing 0 and 5.2 ms (first four bins) and the jittered mean and dividing it by the

926   jittered standard deviation. The inhibitory strength was computed in a similar manner by

927   looking at the trough of the cross correlogram within 0 and 5.2 ms.

928

929   <u>Parameter Optimization</u>

930   Network model parameters were optimized using an evolutionary algorithm to fit

931   measures of network frequency, mean phase coherence, integration and complexity

932   computed from the experimental unit spiking data collected during the 0%, 2%,4% and

933   6% desflurane exposure sessions. The optimized parameters were the synaptic

934   conductance scaling parameters $P_{AMPA}, P_{NMDA}, P_{GABA}$ (A series) and, additionally to those,

935   the maximal conductance of the M-type K+ current g_{Ks} (B series). The algorithm is similar

936   to typical differential evolution procedures[66,67]. Briefly, from a population of 30 agents

937   (parameter sets), at each generation the 10 agents with highest cost function values were

938   replaced with 10 new parameter sets constructed by an evolutionary algorithm described

939   below (Fig 11A). The stopping criteria was 100 generations without change in the lowest

940   cost function ($L(X)$) value across the population of 30 agents.

941

942   The initial population of 30 parameter sets representing the 0% anesthetic state was

943   chosen from the 256 parameter sets generated by assigning parameter values from the

944   following sets: $P_{AMPA}, P_{NMDA} \in \{0.5, 1.0, 1.5, 2.0\}$, $P_{GABA} \in \{2.5, 5.0, 7.5, 10.5\}$ and $g_{Ks} \in$

945     $\{0.3, 0.7, 1.1, 1.5\}\ mS/cm^2$. Model networks with fixed connectivity structure and synaptic

946   strength g_0 values were simulated with each parameter set for 20 s and frequency, mean

947   phase coherence, integration, and complexity measures were computed based on spiking

948   activity excluding the initial 1s, to avoid initial transients . The cost or loss function, $L(X)$,

949   based on these measures, $x =$ frequency, MPC, I(X) and C(X), compared values

950   computed from simulations, x_{sim}, and experimental data, x_{exp}, at 0% anesthetic state as

951   follows:

952
$$L(X) = \sum_x m_x, \qquad m_x = \left(\frac{x_{exp} - x_{sim}}{x_{exp}}\right)^2.$$

953   The 20 lowest cost parameter sets were kept and each parameter value was randomly

954   varied uniformly by 10% of its value to avoid duplicate values. The final 10 parameter sets

955   were then constructed using the differential evolution algorithm.

956

957   Similar to typical differential evolution procedures [66,67] we set a cross over probability

958   CR = 0.8 and a differential weight DW = 2. From the subpopulation of 20 parameter sets,

959   10 randomly chosen sets, $a^k\ (k = 1, ...,10)$, formed the basis for 10 newly created sets,

960 e^k ($k = 1, ..., 10$). For each set a^k, 3 different sets b^k, c^k and $\boldsymbol{d^k}$ were chosen that were

961 different from a^k and each other. Then, for each element $i = 1, ..., 4$ in the set, a random

962 number ρ_i from the uniform distribution [0,1] was chosen. If ρ_i was less than CR, a new

963 parameter value e_i^k was generated as $e_i^k = b_i^k + DW\left(c_i^k - d_i^k\right)$; otherwise $e_i^k = a_i^k$.

964 This was done for each element in the new agent and was repeated until 10 new agents

965 were created. After this was done the 10 new agents were simulated and then the 30 total

966 parameters were evaluated for their cost. The 10 with the highest cost (worse fit) were

967 then rejected and the process was repeated.

968

969 We performed 2 parameter optimizations, A-Series and B-Series, to parse out potentially

970 different effects of anesthetic modulation on synaptic conductances only (A series) and

971 of combined modulation on synaptic conductances and cholinergic effects (B series) (Fig

972 11 B,C). In both scenarios, populations A1/B1 were the result of optimizing

973 $P_{AMPA}, P_{NMDA}, P_{GABA}, g_{Ks}$ to the experimental 0% anesthetic case. In the A-series,

974 P_{NMDA}, P_{GABA} were optimized while in the B-series, $P_{NMDA}, P_{GABA}, g_{Ks}$ were optimized to the

975 2%, 4% and 6% anesthetic cases. Optimizations for the 6% anesthetic case, A4/B4, were

976 initiated from parameter values constrained by experimental reports of 20% average

977 decrease in NMDA-mediated synaptic signaling and 40% increase in GABA-ergic

978 synaptic signaling under desflurane [68,69]. These initial values were randomly varied

979 uniformly by +/- 5% to generate variability in the event of parameter convergence. In the

980 optimizations for the 2% and 4% anesthetic cases, A2/B2 and A3/B3, respectively, the

981 initial population for A2/B2 was A1/B1, and the initial population for A3/B3 was A4/B4.
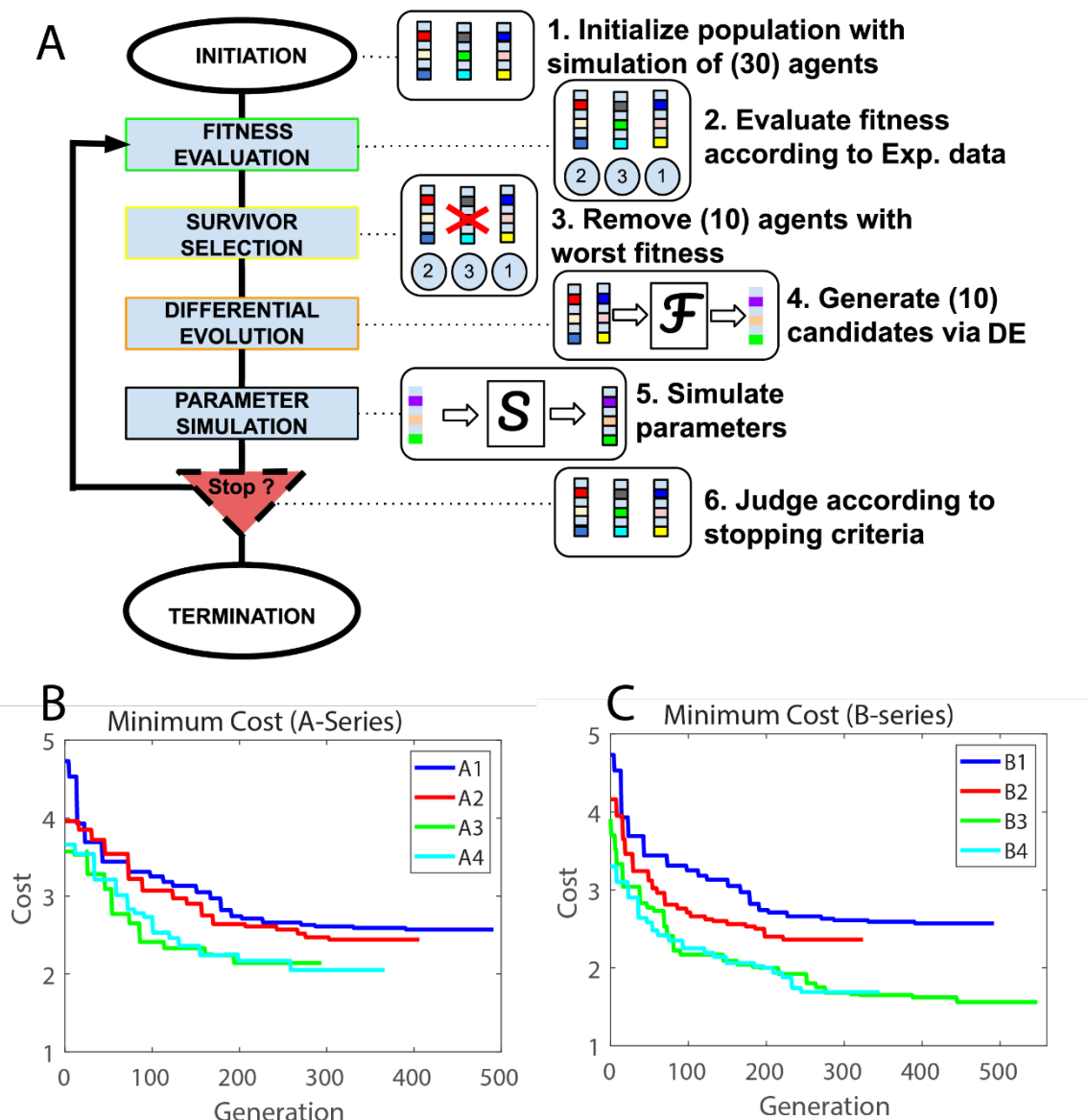
982

Fig 11. Parameter search fine-tuned through Differential Evolution algorithm A) Evolutionary algorithm procedure, differential evolution, was used to optimize model parameters. For each generation, 10 agents (parameter sets) with the highest cost function from the population of 30, were chosen for replacement. Algorithm was repeated until stopping criteria of 100 generations without change in lowest cost function value across the population was met. **B,C)** Lowest cost function values across the parameter set populations at each generation for the A-series (B) and B-series (C) parameter optimizations. Population A1/B1, A2/B2, A3/B3 and A4/B4 were optimized to experimental data from the 0%, 2% ,4% and 6% anesthetic cases, respectively. The optimizations for A1 and B1 were identical. In the A-series (A2-A4), $P_{NDMA, }$ $P_{GABA,}$ were optimized and in the B-Series (B2-B4), $P_{NDMA,}$ $P_{GABA,}$ g_{Ks} were varied

.

997   Simulation of ACh reversal

998   To validate robustness of the parameter optimization, we ran our optimization for 10

999   network realizations, keeping the network structure fixed for all anesthetic levels. The

1000   average and error (SEM) for the optimized parameters across these 10 networks is shown

1001   in Table 1. Table 2 lists the parameter values with the lowest cost function for one of these

1002   optimization runs that we used in our model analysis.

1003

1004   Simulated cholinergic reversal (AR1-AR4/BR1-BR4) was modeled by decreasing the

1005   value of g_{Ks} from the values in A4/B4 to 0.4 mS/cm^2 such that there were 4 values in the

1006   reversal series.

1007

1008   Simulations

1009   Custom C++ code was developed for numerical simulations which was run on the

1010   Greatlakes High Performance Cluster. For the evolutionary algorithm each model

1011   simulation was run for 20s. The stopping criteria was met when the lowest minimum cost

1012   remained unchanged for 100 generations. To check the robustness of the current

1013   parameter set, 10 additional generations were run with model simulations of 80s and an

1014   increased crossover probability (CR=0.9). We detected no change in the minimum cost

1015   parameter set. For the results shown in Figs 3-5 each simulation was simulated for

1016   150000 ms or 150 s. The length of this runtime was necessary to result in enough spike

1017   times to calculate metrics based on cross correlograms. Results in Figs 4 and 5 are for

1018   10 simulation runs in which network connectivity was randomized across runs but

1019   maintained for the different simulated anesthetic levels. In this way, each of the 10

1020   simulation runs corresponds to a unique simulated experiment. On each run the voltage

1021   and gating variables were subject to random initial conditions independent of the network

1022   seed. On initialization V was uniformly varied between [-72,-32] mV, n between [0.2,0.6],

1023   z between [0.2,0.3] and h between [0.2, 0.6] while m was initialized at 0 for all runs. The

1024   equations were integrated using the 4th order Runge Kutta method.

1025

1026   **<u>Acknowledgements</u>**

1033

1034

References

1. Alkire MT, Miller J. General anesthesia and the neural correlates of consciousness. Prog Brain Res. 2005;150: 229–244. doi:10.1016/S0079-6123(05)50017-7

2. Schwartz RS, Brown EN, Lydic R, Schiff ND. Mechanisms of Disease General Anesthesia, Sleep, and Coma. N Engl J Med. 2010;363: 2638–50. doi:10.1056/NEJMra0808281

3. Mashour GA, Hudetz AG. Neural Correlates of Unconsciousness in Large-Scale Brain Networks. Trends Neurosci. 2018;41: 150–160. doi:10.1016/j.tins.2018.01.003

4. Franks NP. General anaesthesia: From molecular targets to neuronal pathways of sleep and arousal. Nat Rev Neurosci. 2008;9: 370–386. doi:10.1038/nrn2372

5. Liang Z, Huang C, Li Y, Hight DF, Voss LJ, Sleigh JW, et al. Emergence EEG pattern classification in sevoflurane anesthesia. Physiol Meas. 2018;39. doi:10.1088/1361-6579/aab4d0

6. Taub AH, Katz Y, Lampl I. Cortical balance of excitation and inhibition is regulated by the rate of synaptic activity. J Neurosci. 2013;33: 14359–14368. doi:10.1523/JNEUROSCI.1748-13.2013

7. Alkire MT, Hudetz AG, Tononi G. Consciousness and anesthesia. Science (80-). 2008;322: 876–880. doi:10.1126/science.1149213

8. Vizuete JA, Pillay S, Diba K, Ropella KM, Hudetz AG. Monosynaptic functional connectivity in cerebral cortex during wakefulness and under graded levels of anesthesia. Front Integr Neurosci. 2012;6: 90. doi:10.3389/fnint.2012.00090

1058 9.   Tononi G, Boly M, Massimini M, Koch C. Integrated information theory: From

1059   consciousness to its physical substrate. Nat Rev Neurosci. 2016;17: 450–461.

1060   doi:10.1038/nrn.2016.44

1061 10.   Hudetz AG. General Anesthesia and Human Brain Connectivity. Brain Connect.

1062   2012;2: 291–302. doi:10.1089/brain.2012.0107

1063 11.   Reed SJ, Plourde G, Tobin S, Chapman CA. Partial antagonism of propofol

1064   anaesthesia by physostigmine in rats is associated with potentiation of fast (80-

1065   200 Hz) oscillations in the thalamus. Br J Anaesth. 2013;110: 646–653.

1066   doi:10.1093/bja/aes432

1067 12.   Solt K, Van Dort CJ, Chemali JJ, Taylor NE, Kenny JD, Brown EN. Electrical

1068   stimulation of the ventral Tegmental area induces reanimation from general

1069   anesthesia. Anesthesiology. 2014;121: 311–319.

1070   doi:10.1097/ALN.0000000000000117

1071 13.   Guidera JA, Taylor NE, Lee JT, Vlasov KY, Pei JZ, Stephen EP, et al.

1072   Sevoflurane induces coherent slow-delta oscillations in rats. Front Neural Circuits.

1073   2017;11. doi:10.3389/fncir.2017.00036

1074 14.   Markram H, Muller E, Ramaswamy S, Reimann MW, Abdellah M, Sanchez CA, et

1075   al. Reconstruction and Simulation of Neocortical Microcircuitry. Cell. 2015;163:

1076   456–492. doi:10.1016/j.cell.2015.09.029

1077 15.   Alkire MT, McReynolds JR, Hahn EL, Trivedi AN. Thalamic microinjection of

1078   nicotine reverses sevoflurane-induced loss of righting reflex in the rat.

1079   Anesthesiology. 2007;107: 264–272. doi:10.1097/01.anes.0000270741.33766.24

1080 16.   Hudetz AG, Wood JD, Kampine JP. Cholinergic Reversal of Isoflurane Anesthesia

1081   in Rats as Measured by Cross-approximate Entropy of the Electroencephalogram.

1082   Anesthesiology. 2003;99: 1125–1131. doi:10.1097/00000542-200311000-00019

1083   17.   Pal D, Dean JG, Liu T, Li D, Watson CJ, Hudetz AG, et al. Differential Role of

1084   Prefrontal and Parietal Cortices in Controlling Level of Consciousness. Curr Biol.

1085   2018;28: 2145-2152.e5. doi:10.1016/j.cub.2018.05.025

1086   18.   Barbero-Castillo A, Mateos-Aparicio P, Porta LD, Camassa A, Perez-Mendez L,

1087   Sanchez-Vives M V. Impact of gabaa and gabab inhibition on cortical dynamics

1088   and perturbational complexity during synchronous and desynchronized states. J

1089   Neurosci. 2021;41: 5029–5044. doi:10.1523/JNEUROSCI.1837-20.2021

1090   19.   Joo DT, Gong D, Sonner JM, Jia Z, Macdonald JF, Eger EI, et al. Blockade of

1091   AMPA Receptors and Volatile Anesthetics Reduced Anesthetic Requirements in

1092   GluR2 Null Mutant Mice for Loss of the Righting Reflex and Antinociception but

1093   Not Minimum Alveolar Concentration. Anesthesiology. 2001.

1094   doi:10.1097/00000542-200103000-00020

1095   20.   Rudolph U, Antkowiak B. Molecular and neuronal substrates for general

1096   anaesthetics. Nat Rev Neurosci. 2004;5: 709–720. doi:10.1038/nrn1496

1097   21.   Roach JP, Eniwaye B, Booth V, Sander LM, Zochowski MR. Acetylcholine

1098   Mediates Dynamic Switching Between Information Coding Schemes in Neuronal

1099   Networks. Front Syst Neurosci. 2019;13. doi:10.3389/fnsys.2019.00064

1100   22.   Tononi G. Consciousness, information integration, and the brain. Prog Brain Res.

1101   2005;150: 109–126. doi:10.1016/S0079-6123(05)50009-8

1102   23.   Fujisawa S, Amarasingham A, Harrison MT, Buzsáki G. Behavior-dependent

1103   short-term assembly dynamics in the medial prefrontal cortex. Nat Neurosci.

1104   2008;11: 823–833. doi:10.1038/nn.2134

1105   24.   Hudetz AG, Vizuete JA, Imas OA. Desflurane selectively suppresses long-latency

1106   cortical neuronal response to flash in the rat. Anesthesiology. 2009.

1107   doi:10.1097/ALN.0b013e3181ab671e

1108   25.   Pappas I, Adapa RM, Menon DK, Stamatakis EA. Brain network disintegration

1109   during sedation is mediated by the complexity of sparsely connected regions.

1110   Neuroimage. 2019;186: 221–233. doi:10.1016/j.neuroimage.2018.10.078

1111   26.   Pal D, Li D, Dean JG, Brito MA, Liu T, Fryzel AM, et al. Level of consciousness is

1112   dissociable from electroencephalographic measures of cortical connectivity, slow

1113   oscillations, and complexity. J Neurosci. 2020;40: 605–618.

1114   doi:10.1523/JNEUROSCI.1910-19.2019

1115   27.   Hashemi M, Hutt A, Buhry L, Sleigh J. Optimal Model Parameter Estimation from

1116   EEG Power Spectrum Features Observed during General Anesthesia.

1117   Neuroinformatics. 2018;16: 231–251. doi:10.1007/s12021-018-9369-x

1118   28.   Hutt A. The population firing rate in the presence of GABAergic tonic inhibition in

1119   single neurons and application to general anaesthesia. Cogn Neurodyn. 2012;6:

1120   227–237. doi:10.1007/s11571-011-9182-9

1121   29.   Sleigh JW, Voss L, Steyn-Ross ML, Steyn-Ross DA, Wilson MT. Modelling Sleep

1122   and General Anaesthesia. Sleep Anesth. 2011;15: 21–41. doi:10.1007/978-1-

1123   4614-0173-5_2

1124   30.   Sleigh JW, Vizuete JA, Voss L, Steyn-Ross A, Steyn-Ross M, Marcuccilli CJ, et

1125   al. The electrocortical effects of enflurane: Experiment and theory. Anesth Analg.

1126   2009;109: 1253–1262. doi:10.1213/ANE.0b013e3181add06b

1127   31.   Bukoski A, Steyn-Ross DA, Pickett AF, Steyn-Ross ML. Anesthesia modifies

1128   subthreshold critical slowing down in a stochastic Hodgkin-Huxley-like model with

1129   inhibitory synaptic input. Phys Rev E. 2018;97. doi:10.1103/PhysRevE.97.062403

1130   32.   Storer KP, Reeke GN. γ-Aminobutyric acid receptor type a receptor potentiation

1131   reduces firing of neuronal assemblies in a computational cortical model.

1132   Anesthesiology. 2012;117: 780–790. doi:10.1097/ALN.0b013e318269ba6d

1133   33.   Buzsáki G, Mizuseki K. The log-dynamic brain: How skewed distributions affect

1134   network operations. Nat Rev Neurosci. 2014;15: 264–278. doi:10.1038/nrn3687

1135   34.   Banks MI, Krause BM, Endemann CM, Campbell DI, Kovach CK, Dyken ME, et

1136   al. Cortical functional connectivity indexes arousal state during sleep and

1137   anesthesia. Neuroimage. 2020;211: 116627.

1138   doi:10.1016/j.neuroimage.2020.116627

1139   35.   Kim M, Mashour GA, Moraes SB, Vanini G, Tamal V, Janke E, et al. Functional

1140   and topological conditions for explosive synchronization develop in human brain

1141   networks with the onset of anesthetic-induced unconsciousness. Front Comput

1142   Neurosci. 2016;10. doi:10.3389/fncom.2016.00001

1143   36.   Borisyuk R, Borisyuk G. Synchronization of neural activity and models of

1144   information processing in the brain. Behav Brain Sci. 1998;21: 833–833.

1145   doi:doi:10.1017/S0140525X98241768

1146   37.   Matias FS, Carelli P V., Mirasso CR, Copelli M. Anticipated synchronization in

1147   neuronal circuits unveiled by a phase-response-curve analysis. Phys Rev E.

1148   2017;95: 052410. doi:10.1103/PhysRevE.95.052410

1149   38.   Simonov AY, Gordleeva SY, Pisarchik AN, Kazantsev VB. Synchronization with

1150   an arbitrary phase shift in a pair of synaptically coupled neural oscillators. JETP

1151   Lett. 2014;98: 632–637. doi:10.1134/S0021364013230136

1152 39. Buzsáki G, Wang X-J. Mechanisms of gamma oscillations. Annu Rev Neurosci.

1153   2012;35: 203–225. doi:10.1146/annurev-neuro-062111-150444

1154 40. Lu Y, Sarter M, Zochowski M, Booth V. Phasic cholinergic signaling promotes

1155   emergence of local gamma rhythms in excitatory–inhibitory networks. Eur J

1156   Neurosci. 2020;52: 3545–3560. doi:10.1111/ejn.14744

1157 41. Panzeri S, Macke JH, Gross J, Kayser C. Neural population coding: Combining

1158   insights from microscopic and mass signals. Trends Cogn Sci. 2015;19: 162–172.

1159   doi:10.1016/j.tics.2015.01.002

1160 42. Rich S, Zochowski M, Booth V. Effects of Neuromodulation on Excitatory–

1161   Inhibitory Neural Network Dynamics Depend on Network Connectivity Structure. J

1162   Nonlinear Sci. 2020;30: 2171–2194. doi:10.1007/s00332-017-9438-6

1163 43. Stiefel KM, Gutkin BS, Sejnowski TJ. Cholinergic neuromodulation changes

1164   phase response curve shape and type in cortical pyramidal neurons. PLoS One.

1165   2008;3. doi:10.1371/journal.pone.0003947

1166 44. Stiefel KM, Gutkin BS, Sejnowski TJ. The effects of cholinergic neuromodulation

1167   on neuronal phase-response curves of modeled cortical neurons. J Comput

1168   Neurosci. 2009;26: 289–301. doi:10.1007/s10827-008-0111-9

1169 45. Fink CG, Booth V, Zochowski M. Cellularly-driven differences in network

1170   synchronization propensity are differentially modulated by firing frequency. PLoS

1171   Comput Biol. 2011;7. doi:10.1371/journal.pcbi.1002062

1172 46. Roach JP, Sander LM, Zochowski MR. Memory recall and spike-frequency

1173   adaptation. Phys Rev E. 2016. doi:10.1103/PhysRevE.93.052307

1174   47.   Lendner JD, Helfrich RF, Mander BA, Romundstad L, Lin JJ, Walker MP, et al. An

1175   electrophysiological marker of arousal level in humans. Elife. 2020;9: 1–29.

1176   doi:10.7554/eLife.55092

1177   48.   Tononi G, Sporns O, Edelman GM. A measure for brain complexity: Relating

1178   functional segregation and integration in the nervous system. Neurobiology. 1994.

1179   49.   Luo T, Leung LS. Basal Forebrain Histaminergic Transmission Modulates

1180   Electroencephalographic Activity and Emergence from Isoflurane Anesthesia.

1181   Anesthesiology. 2009;111: 725–733. doi:10.1097/ALN.0b013e3181b061a0

1182   50.   Nelson LE, Guo TZ, Lu J, Saper CB, Franks NP, Mazel M. The sedative

1183   component of anesthesia is mediated by GABAA receptors in an endogenous

1184   sleep pathway. Nat Neurosci. 2002;5: 979–984. doi:10.1038/nn913

1185   51.   Xie G, Deschamps A, Backman SB, Fiset P, Chartrand D, Dagher A, et al. Critical

1186   involvement of the thalamus and precuneus during restoration of consciousness

1187   with physostigmine in humans during propofol anaesthesia: A positron emission

1188   tomography study. Br J Anaesth. 2011;106: 548–557. doi:10.1093/bja/aeq415

1189   52.   Kasuga T, Meno A, Honda M, Momoeda K, Nagase M, Hanaoka K. [General

1190   anesthesia for two patients taking methylphenidate (Ritalin)]. Masui. 2008;57:

1191   748–751. Available: http://europepmc.org/abstract/MED/18546908

1192   53.   Solt K, Cotten JF, Cimenser A, Wong KFK, Chemali JJ, Brown EN.

1193   Methylphenidate actively induces emergence from general anesthesia.

1194   Anesthesiology. 2011;115: 791–803. doi:10.1097/ALN.0b013e31822e92e5

1195   54.   Li Y, Chen D, Wang H, Wang Z, Song F, Li H, et al. Intravenous versus Volatile

Anesthetic Effects on Postoperative Cognition in Elderly Patients Undergoing

Laparoscopic Abdominal Surgery: A Multicenter, Randomized Trial.

Anesthesiology. 2021; 381–394. doi:10.1097/ALN.0000000000003680

55. Ching S, Cimenser A, Purdon PL, Brown EN, Kopell NJ. Thalamocortical model

for a propofol-induced α-rhythm associated with loss of consciousness. Proc Natl

Acad Sci U S A. 2010;107: 22665–22670. doi:10.1073/pnas.1017069108

56. Hindriks R, van Putten MJAM. Meanfield modeling of propofol-induced changes in

spontaneous EEG rhythms. Neuroimage. 2012;60: 2323–2334.

doi:10.1016/j.neuroimage.2012.02.042

57. Bojak I, Liley DTJ. Modeling the effects of anesthesia on the

electroencephalogram. Phys Rev E - Stat Nonlinear, Soft Matter Phys. 2005;71:

1–22. doi:10.1103/PhysRevE.71.041902

58. Flores FJ, Hartnack KE, Fath AB, Kim SE, Wilson MA, Brown EN, et al.

Thalamocortical synchronization during induction and emergence from propofol-

induced unconsciousness. Proc Natl Acad Sci U S A. 2017;114: E6660–E6668.

doi:10.1073/pnas.1700148114

59. Moran RJ, Jung F, Kumagai T, Endepols H, Graf R, Dolan RJ, et al. Dynamic

causal models and physiological inference: A validation study using isoflurane

anaesthesia in rodents. PLoS One. 2011;6. doi:10.1371/journal.pone.0022790

60. Hudetz AG, Vizuete JA, Pillay S, Ropella KM. Critical Changes in Cortical

Neuronal Interactions in Anesthetized and Awake Rats. Anesthesiology.

2015;123: 171–180. doi:10.1097/ALN.0000000000000690

61. Hodgkin AL, Huxley AF. A Quantitative Description of Membrain current and its

1219   application to conduction and excitation in nerve. J Physiol. 1952;117: 500–544.

1220   doi:10.1109/ICCCT2.2017.7972284

1221 62. Jacobs AL, Fridman G, Douglas RM, Alam NM, Latham PE, Prusky GT, et al.

1222   Ruling out and ruling in neural codes. Proc Natl Acad Sci. 2009;106: 5936–5941.

1223   doi:https://doi.org/10.1073/pnas.0900573106

1224 63. Mofakham S, Fink CG, Booth V, Zochowski MR. Interplay between excitability

1225   type and distributions of neuronal connectivity determines neuronal network

1226   synchronization. Phys Rev E. 2016;94. doi:10.1103/PhysRevE.94.042427

1227 64. Moradi K, Moradi K, Ganjkhani M, Hajihasani M, Gharibzadeh S, Kaka G. A fast

1228   model of voltage-dependent NMDA receptors. J Comput Neurosci. 2013;34: 521–

1229   531. doi:10.1007/s10827-012-0434-4

1230 65. Wang H, Stradtman GG, Wang X-J, Gao W-J. A specialized NMDA receptor

1231   function in layer 5 recurrent microcircuitry of the adult rat prefrontal cortex. Proc

1232   Natl Acad Sci. 2008;105: 16791 LP – 16796. doi:10.1073/pnas.0804318105

1233 66. Das S, Suganthan PN. Differential evolution: A survey of the state-of-the-art. IEEE

1234   Trans Evol Comput. 2011;15: 4–31. doi:10.1109/TEVC.2010.2059031

1235 67. Storn R, Price K. Differential Evolution-A Simple and Efficient Heuristic for Global

1236   Optimization over Continuous Spaces. J Glob Optim. Kluwer Academic

1237   Publishers; 1997. doi:https://doi.org/10.1023/A:1008202821328

1238 68. Mapelli J, Gandolfi D, Giuliani E, Prencipe FP, Pellati F, Barbieri A, et al. The

1239   effect of desflurane on neuronal communication at a central synapse. PLoS One.

1240   2015;10. doi:10.1371/journal.pone.0123534

1241 69. Xu X, Zheng C, Li N, Shen H, Wang G. The decrease of NMDAR subunit

1242   expression and NMDAR EPSC in hippocampus by neonatal exposure to

1243   desflurane in mice. Behav Brain Res. 2017;317: 82–87.

1244   doi:10.1016/j.bbr.2016.09.035

1245

1246   **Supporting Information**

1247   **S1 Fig**. **B-Series effects of anesthetic concentration and simulated ACh-induced**

1248   **reversal on relative profiles of neuronal firing frequency.** Each panel depicts the firing

1249   frequency of each neuron in a given anesthetic/reversal state (x-axis) compared to its

1250   firing frequency in the non-anesthetic condition (B1) (y-axis) A,B) Neurons in B series

1251   optimized networks and reversal.